THE STELLAR MASS ASSEMBLY OF GALAXIES FROM z = 0 TO z = 4: ANALYSIS OF A SAMPLE SELECTED IN THE REST-FRAME NEAR-INFRARED WITH SPITZER

Pablo G. Pérez-González,[1,2] George H. Rieke,[3] Victor Villar,[1] Guillermo Barro,[1]
Myra Blaylock,[3] Eiichi Egami,[3] Jesús Gallego,[1] Armando Gil de Paz,[1]
Sergio Pascual,[1] Jaime Zamorano,[1] and Jennifer L. Donley[3]

ABSTRACT

Using a sample of ∼28,000 sources selected at 3.6–4.5 μm with *Spitzer* observations of the Hubble Deep Field North, the Chandra Deep Field South, and the Lockman Hole (surveyed area ∼664 arcmin^2), we study the evolution of the stellar mass content of the universe at $0 < z < 4$. We calculate stellar masses and photometric redshifts, based on ∼2000 templates built with stellar population and dust emission models fitting the ultraviolet to mid-infrared spectral energy distributions of galaxies with spectroscopic redshifts. We estimate stellar mass functions for different redshift intervals. We find that 50% of the local stellar mass density was assembled at $0 < z < 1$ (average star formation rate [SFR] 0.048 $M_\odot$ yr^{-1} Mpc^{-3}), and at least another 40% at $1 < z < 4$ (average SFR 0.074 $M_\odot$ yr^{-1} Mpc^{-3}). Our results confirm and quantify the "downsizing" scenario of galaxy formation. The most massive galaxies ($M > 10^{12.0} M_\odot$) assembled the bulk of their stellar content rapidly (in 1–2 Gyr) beyond $z \sim 3$ in very intense star formation events (producing high specific SFRs). Galaxies with $10^{11.5} < M < 10^{12.0} M_\odot$ assembled half of their stellar mass before $z \sim 1.5$, and more than 90% of their mass was already in place at $z \sim 0.6$. Galaxies with $M < 10^{11.5} M_\odot$ evolved more slowly (presenting smaller specific SFRs), assembling half of their stellar mass below $z \sim 1$. About 40% of the local stellar mass density of $10^{9.0} < M < 10^{11.0} M_\odot$ galaxies was assembled below $z \sim 0.4$, most probably through accretion of small satellites producing little star formation. The cosmic stellar mass density at $z > 2.5$ is dominated by optically faint ($R \gtrsim 25$) red galaxies (distant red galaxies or *BzK* sources), which account for ∼30% of the global population of galaxies, but contribute at least 60% of the cosmic stellar mass density. Bluer galaxies (e.g., Lyman break galaxies) are more numerous but less massive, contributing less than 50% of the global stellar mass density at high redshift.

Subject headings: galaxies: evolution — galaxies: high-redshift — galaxies: photometry — galaxies: starburst — infrared: galaxies

Online material: color figures, machine-readable table

1. INTRODUCTION

In the last decade, our knowledge about the formation and evolution of galaxies has increased significantly, with the advent of deep and/or wide photometric and spectroscopic galaxy surveys carried out at different wavelengths. This advance in our understanding of the evolution of the universe is succinctly represented in the so-called Lilly-Madau plot (Lilly et al. 1996; Madau et al. 1996), a diagram showing the evolution of the star formation rate (SFR) density of the universe as a function of look-back time (or redshift). Originally, with only a few points in the diagram, it was clearly visible that in the last ∼8 Gyr (i.e., about 55% of its age), the universe experienced a significant decrease (of about a factor of 10) in the rate at which new stars were created. Now, there are more than 80 data points in the Lilly-Madau diagram (see Hopkins 2004 for a nice compilation of results on this topic; see also Schiminovich et al. 2005, Pérez-González et al. 2005, and Hopkins & Beacom 2006), and the picture is clearer at $z \lesssim 1$, where there is just a factor of 2 scatter among the estimations coming from different surveys, and using different selection techniques and SFR tracers. At $z \gtrsim 1$, the uncertainties are larger, up to a factor of ∼5, but there is increasing evidence that the SFR density remained approximately constant for 4–5 Gyr (from $z \sim 1$ to $z \sim 4$).

Although the Lilly-Madau plot concentrates a large amount of information about the formation of structures in the universe, the (recent) SFR is not the best parameter to characterize the evolution of a galaxy, as it is an instantaneous parameter. Indeed, the stellar mass or the metallicity, which are closely linked to the star formation history, are more appropriate parameters to follow the evolution of galaxies. Thus, an increasing number of studies explore the evolution of the cosmic comoving stellar mass density, showing that it has steadily increased in the last 12 Gyr (see, e.g., Brinchmann & Ellis 2000; Dickinson et al. 2003b; Glazebrook et al. 2004; Drory et al. 2005; Fontana et al. 2006; see also the references given in Fig. 5).

Because of the increasingly large scale of cosmological surveys, the problem of the evolution of galaxies is now being addressed by dividing the samples into ranges in stellar mass. In this context, the evolution of galaxies seems to follow a "downsizing" scenario (Cowie et al. 1996), in which the most massive galaxies are formed first and the star formation continues in less massive systems until more recent epochs (Heavens et al. 2004; Juneau et al. 2005; Bauer et al. 2005; Pérez-González et al. 2005; Bundy et al. 2006; Tresse et al. 2007). Although the downsizing picture is being confirmed by an increasing number of works, the quantification of the process is still very limited, given the necessity of large samples of high-redshift galaxies with multiwavelength data to explore it (covering from the rest-frame ultraviolet to the near-infrared and beyond).

[1] Departamento de Astrofísica, Facultad de CC. Físicas, Universidad Complutense de Madrid, E-28040 Madrid, Spain.
[2] Associate Astronomer at Steward Observatory, University of Arizona.
[3] Steward Observatory, University of Arizona, 933 North Cherry Avenue, Tucson, AZ 85721.

In contrast to these observational results, classical models of galaxy evolution assuming a cold dark matter (CDM) universe usually predict that the most massive galaxies assembled late, via the coalescence of small halos that form larger ones (e.g., Kauffmann et al. 1993; Baugh et al. 1998; Somerville et al. 2001). This contradicts the observational evidence of the existence of large galaxies at high redshifts (some of them already harboring old stellar populations at those early epochs, some with significant recent star formation), detected by their unusually red colors (see, e.g., Elston et al. 1988; Dey et al. 1999; Dickinson et al. 2000; Im et al. 2002; Franx et al. 2003) or their bright emission at submillimeter wavelengths (e.g., Smail et al. 1997; Hughes et al. 1998; see also Blain et al. 2002 for a review). More recent models based on a ΛCDM cosmology succeed in predicting the early formation of massive galaxies by introducing very large dust extinctions, nonstandard initial mass functions, and/or suppression of the star formation due to the quenching of cooling flows by supernovae or active galactic nuclei (e.g., Cole et al. 2000; Granato et al. 2004; Baugh et al. 2005; Nagamine et al. 2005a; Croton et al. 2006; Bower et al. 2006).

In this paper, we observationally characterize the build-up of the stellar mass of galaxies in the last $\sim$12 Gyr (almost 90% of the age of the universe) as a function of the stellar mass of each object. This is done by estimating stellar mass functions at different redshifts. Given that we are interested in the stellar mass assembly of galaxies, it would be convenient to analyze a sample whose selection is based precisely on that parameter, the stellar mass. From studies at low and intermediate redshift, we know that the rest-frame near-infrared (NIR) emission of galaxies arises mainly from relatively old stars that usually dominate the total stellar mass of galaxies, in contrast to younger stellar populations, which may contribute little to the rest-frame NIR emission and stellar mass, but emit strongly at bluer wavelengths. Indeed, stellar mass estimations based (only) on photometry at rest-frame wavelengths bluer than $\sim$600 nm are particularly troublesome, because of the ability of a small population of young stars to dominate the output of a galaxy. In the red and NIR, the light is dominated by similar stellar populations, but the rest-frame NIR is preferred for estimating stellar masses because of its relative immunity to extinction. In addition, data at red wavelengths is crucial to detecting galaxies that are very faint in the optical (too faint for optical surveys) but may contribute significantly to or even dominate the stellar mass density of the universe at high z (e.g., extremely red objects [EROs]; Elston et al. 1988, Yan et al. 2000; or distant red galaxies [DRGs]; Franx et al. 2003, van Dokkum et al. 2003). These galaxies are usually missed by selection techniques based on rest-frame ultraviolet colors (e.g., Lyman break galaxies [LBGs]; Steidel et al. 2003). Therefore, a sample selected in the rest-frame NIR is the most adequate to attempt a stellar mass function analysis. Still, mass-to-light ratios in the rest-frame NIR from galaxy to galaxy may still vary by factor of 6–15 (depending on the mean age of the stellar population, the presence of recent bursts, etc.; see, e.g., Bell & de Jong 2001, Shapley et al. 2005, or Labbé et al. 2005). This means that a complete study of the optical-to-NIR spectral energy distribution of galaxies on a galaxy-by-galaxy basis should be performed to obtain robust stellar mass estimates.

This paper is based on the analysis of a sample of galaxies at $0 < z < 4$ selected in three different fields (to minimize cosmic variance problems) at 3.6–4.5 μm with the Infrared Array Camera (IRAC; Fazio et al. 2004b) on board the *Spitzer Space Telescope* (Werner et al. 2004). Even at the highest redshift in the sample, the sources are still selected in the rest-frame NIR (approx-

imately the J band), so an IRAC selected sample uniquely constitutes a statistically complete sample in stellar mass at all redshifts up to $z \sim 4$ (to a certain lower limit based on the flux cut of the sample). In addition, the estimations of the stellar masses of our galaxies always count with a NIR band, which significantly reduces the uncertainties in the derived stellar masses (see, e.g., Fontana et al. 2006), since the relatively old stellar population contributing the most to the total stellar mass of galaxies usually dominates the emission at NIR wavelengths, and also because the NIR is relatively free of extinction effects and hence is better for estimating stellar masses than shorter wavelengths. Our sample selection constitutes an extension (in area, depth, and consequently number of galaxies detected) of those used by other groups based on ground-based K-band data (e.g., Drory et al. 2004; Fontana et al. 2004).

This paper is organized as follows. Section 2 presents the data set and samples of galaxies used in this work. Section 3 describes the stellar population and dust emission models used to estimate photometric redshifts, stellar masses, and SFRs for all galaxies in our sample. Here we also discuss the uncertainties in these parameters. Sections 4 and 5 discuss the main results for photometric redshifts and stellar masses. More precisely, we present stellar mass functions and densities, discussing their evolution with redshift. Section 6 divides our sample into several subtypes (such as DRGs or LBGs), and discusses the evolution of galaxies of different natures and their role in the evolution of the stellar mass density of the universe as a whole. Section 7 analyzes the SFRs of the galaxies in our sample and the evolution of the cosmic SFR density. Finally, § 8 summarizes the conclusions of this paper.

Throughout this paper, we use a cosmology with $H_0 = 70$ km s^{-1} Mpc^{-1}, $\Omega_M = 0.3$, and $\Lambda = 0.7$. All magnitudes refer to the AB system. The results for stellar masses assume a Salpeter (1955) universal (i.e., constant through time) initial mass function (IMF) with $0.1 < M < 100$ $M_\odot$ and a single power-law slope in this range.

2. SAMPLE SELECTION

This paper analyzes the main properties of the galaxies selected by IRAC (hereafter the IRAC selected sample), which should be close to a stellar mass selected sample up to the highest redshifts in our survey. We complemented this data set with a sample of galaxies selected in a ground-based optical image (hereafter the I-band selected sample[4]), in order to check the effect on our results of the galaxies missed by IRAC, i.e., galaxies that are relatively faint in the rest-frame NIR but can be detected in deep optical imaging. This sample of NIR-faint galaxies should allow us to probe the stellar mass functions at small masses below the IRAC detection limits (and at higher masses, where the galaxies should also be detected by IRAC).

The IRAC sample is drawn from the *Spitzer* GTO (see, e.g., Pérez-González et al. 2005) and GOODS (Dickinson et al. 2003a) IRAC and MIPS observations of the Hubble Deep Field–North (HDF-N) and the Chandra Deep Field–South (CDF-S), and the *Spitzer* GTO data in the Lockman Hole Field (LHF). In each field, we concentrated on a relatively reduced sky area with the deepest coverage by *Spitzer*, and also observed by other X-ray, ultraviolet

---

[4] For this selection, we chose the deepest ground-based images in a band common (or similar) to the three fields, namely, the Subaru I-band images in the LHF and the HDF-N, and the Subaru NB816 image (close to an I-band image, and also very deep) in the CDF-S.

(UV), optical, near-infrared (NIR), and mid-infrared (MIR) surveys. In the HDF-N, we focused our analysis in 257 arcmin² centered at $\alpha = 12^h38^m56^s, \delta = +62°14'06''$ (J2000.0), and including the entire GOODS ACS footprint; in the CDF-S, we focused on a rectangle of 225 arcmin² centered at $\alpha = 03^h30^m28^s, \delta = -27°48'18''$ (J2000.0), also including the entire GOODS ACS footprint; and in the LHF, we used a square area of 183 arcmin² centered at $\alpha = 10^h52^m47^s, \delta = +57°29'06''$ (J2000.0). This adds up a total surveyed area of 664 arcmin².

The reduction, source extraction, and photometry of the IRAC and MIPS images were performed in the same way as explained in Pérez-González et al. (2005). We describe the procedure with more details in Appendix A. The IRAC sample was built by detecting sources separately in the two bluer IRAC bands (at 3.6 and 4.5 μm), and then merging the catalogs and removing repeated sources. Aperture photometry was measured in the four IRAC images (fixing the positions and forcing the detection in all bands), obtaining the final integrated magnitude after applying an aperture correction based on empirical point-spread functions (PSFs). All the sources in the IRAC sample have measured fluxes at both 3.6 and 4.5 μm. For the MIPS 24 μm images, we measured integrated fluxes using PSF fits and aperture corrections. The *I*-band selected sample was built by detecting sources with SEXTRACTOR (Bertin & Arnouts 1996) in the optical images.

Our IRAC selected sample is composed of 9074 sources in the HDF-N, 9676 in the CDF-S, and 9149 in the LHF, for a total of 27,899 sources (i.e., 42 sources arcmin⁻²). Of these, less than 3% (700 sources) are identified as stars (see the star-galaxy separation method in § A.5). Based on simulations carried out by adding artificial sources to the IRAC images and trying to recover their detection and input flux, we estimate that our IRAC catalogs in the HDF-N and the CDF-S are 75% (90%) complete down to 1.6 μJy (5.0 μJy) at 3.6 μm, and 1.4 μJy (4.0 μJy) at 4.5 μm. For the LHF, where deep GOODS IRAC data are not available, the 75% (90%) completeness levels are 2.2 μJy (5.8 μJy) at 3.6 μm, and 2.0 μJy (4.8 μJy) at 4.5 μm. Above the 75% completeness flux limits, our sample has 7512 galaxies (after removal of stars) in the HDF-N, 6546 galaxies in the CDF-S, and 5341 galaxies in the LHF, adding a total of 19,399 galaxies (29.2 sources arcmin⁻²). Of these, 6686 (35%) galaxies are detected by MIPS at 24 μm, 3483 (18%) above our 75% 24 μm completeness level [$F(24) = 80$ μJy].

We concentrated our analysis of the *I*-band selected sample on the region covered by the other UV-to-MIR surveys, and enclosing a similar number of sources as detected with the IRAC selection (we therefore considered smaller regions in each field). We used an area of 101 arcmin² centered at $\alpha = 12^h37^m00^s, \delta = +62°13'30''$ (J2000.0) in the HDF-N, 103 arcmin² at $\alpha = 03^h32^m28^s, \delta = -27°48'54''$ (J2000.0) in the CDF-S, and 70 arcmin² at $\alpha = 10^h52^m48^s, \delta = +57°29'24''$ in the LHF. The samples are formed by 7326 sources (112 of them identified as stars) in the HDF-N, 6680 (87 stars) in the CDF-S, and 6797 (99 stars) in the LHF, for a total of 20,505 galaxies with $I \lesssim 25.5$ (75 sources arcmin⁻²).

The *Spitzer* data were complemented with other publicly available and proprietary photometric and spectroscopic data in the three fields. These data cover the electromagnetic spectrum from UV to MIR wavelengths. The description of the different data sets and the procedure used to get merged UV-to-MIR photometry for each source is described in detail in Appendix A. The spectral energy distributions (SEDs) of each source were used to remove stars from our sample, detect candidates for harboring an active galactic nucleus (AGN), and to estimate photometric redshifts, stellar masses, and SFRs for the entire sample on a galaxy-by-galaxy basis, as explained in § 3 and Appendix B.

3. ESTIMATION OF PHOTOMETRIC REDSHIFTS, STELLAR MASSES, AND STAR FORMATION RATES

The estimation of the photometric redshift, stellar mass, and SFR of each galaxy in our IRAC and *I*-band selected samples was carried out in a two-step process. Given the significant degeneracies inherent to any stellar population modeling, and in order to get the best estimations of the interesting parameters, we decided to first build a reference set of stellar population and dust emission templates. This trained template set was used in the second step to obtain photometric redshifts, stellar masses, and SFRs for the entire sample. The reference template set was built with the ∼2000 galaxies in our spectroscopic sample with highly reliable redshifts and well-covered SEDs (with enough data points from the rest-frame UV to NIR/MIR wavelengths). This is the same approach we chose in Pérez-González et al. (2005). As a major improvement of our photometric redshift technique described in that paper, we (significantly) increased the spectral resolution of the templates by fitting the SEDs of the galaxies in the reference spectroscopic sample with models of the stellar population and dust emission (probing more than 10^{11} different models).

In Appendix B, we describe the stellar and dust emission modeling procedure, the building of the reference template set, and the procedure used to get photometric redshift, stellar mass, and SFR estimates for each galaxy in our entire sample. In this appendix we also evaluate the goodness of our photometric redshift, stellar mass, and SFR estimates. We show that our photometric redshifts for galaxies at $z < 1.5$ are better than $\sigma_z/(1 + z) < 0.1$ (where σ_z is the absolute value of $\delta z = z_{spec} - z_{photo}$) for approximately 87% of the galaxies in our complete sample, and better than $\sigma_z/(1 + z) < 0.2$ for 95%. At $z > 1.5$, we test our photometric redshifts distributions for different samples of high-redshift galaxies (LBGs, DRGs, and *BzK* sources; see § 6 for more details), obtaining acceptable results, in good agreement with other spectroscopic and photometric redshift analyses.

The distributions of photometric redshift uncertainties (as derived from the comparison with spectroscopic redshifts in Appendix B) for different magnitude and redshift intervals are used in § 5 to estimate the uncertainties in the stellar mass functions. In addition, the redshift intervals in that section and the following are constructed assuming that the typical photometric redshift error is $\sigma_z/(1 + z) \sim 0.1$ (valid for more than 85% of our sample). We would like to stress that the results described in the following sections are more robust at $z < 1.5$, where the photometric redshifts are well tested and the photometry is very accurate, than at $z > 1.5$, where the unavailability of spectroscopic redshifts does not allow as thorough a characterization of the photometric redshifts as at low z, and photometric errors are generally larger.

In Appendix B we also discuss the goodness of our stellar mass estimates. We conclude that the choices of a single population or a two-component population in the stellar emission models, the use of distinct stellar population libraries, different IMFs, or different extinction recipes produce changes in the derived stellar masses of a factor of 2–3, which is also the typical error in any stellar population synthesis analysis, linked to the degeneracies of the solutions to the problem. Therefore, our stellar mass estimates are good within a factor of 2–3.

The estimations of the SFRs for each galaxy are also proved to be good within a factor of 2 in Appendix B, an uncertainty which is consistent with other evaluations of UV- and IR-based SFRs (e.g., Papovich & Bell 2002; Le Floc'h et al. 2005; Caputi et al. 2006).

Finally, Appendix B also discusses the validity of our estimated parameters for galaxies harboring an AGN. We conclude

that photometric redshifts and stellar masses should not be affected dramatically for most AGNs (except for very bright Type 1 AGNs), but IR-based SFRs can be overestimated. For this reason, we exclude AGNs from the analysis of SFRs performed in § 7.2, but we keep most of them (only excluding very bright X-ray sources) in our calculations of the stellar mass functions and densities.

4. REDSHIFT DISTRIBUTION OF OUR SAMPLE

Figure 1 shows the photometric redshift distribution of our IRAC selected sample (average number density and number densities in each field), the subsample also detected by MIPS at 24 μm, and the I-band selected sample. Only sources with fluxes above our 75% completeness levels are included. The distributions have been constructed taking into account the typical photometric redshift error, $\sigma_z/(1 + z) \sim 0.1$, i.e., Figure 1 represents the real redshift distribution convolved with the photometric redshift probability distribution.

Figure 1 demonstrates the importance of cosmic variance effects on deep photometric surveys. Indeed, large-scale structures are clearly visible and located at different redshifts for our three fields, especially at $z \lesssim 1$. Number density variations of up to a factor of 2 can exist at a given redshift from one field to another. The HDF-N shows two very prominent density peaks at $z \sim 0.5$ and $z \sim 0.9$, consistent with the spectroscopic redshift histogram found in Figure 16 of Wirth et al. (2004). There are also minor prominences at $z = 1.5$–2.0 and $z = 2.0$–2.5, which are also seen in the spectroscopic follow-up of UV-selected galaxies in Reddy et al. (2006a). The CDF-S presents very prominent density peaks at $z \sim 0.3$, $z \sim 0.7$, and $z \sim 1.1$ (the latter broadens up to $z \sim 1.4$), which coincides (after convolution with the typical photometric redshift uncertainty) with the most prominent spectroscopically confirmed peaks found in Figure 7 of Vanzella et al. (2006). The LHF shows an enhanced density at $z \lesssim 0.3$ and $z \sim 0.7$–1.0, and a very prominent peak at $z = 1.5$–1.8. These peaks are consistent with the high density of X-ray sources found by Mainieri et al. (2002b) and Zappacosta et al. (2005) at $z \sim 0.8$ and $z \sim 1.6$–1.8, and the analysis of the shallower IRAC SWIRE data in Rowan-Robinson et al. (2005).

Only by combining data for several fields are we able to smooth out cosmic variance effects. Indeed, the average redshift distributions for IRAC sources (Fig. 1, *solid black line*) and MIPS sources (*dashed black line*) are much smoother than the analogous curves for the individual fields. The shape of the redshift distribution for the IRAC sample is typical of a flux-limited sample with a roughly homogeneous detection probability, i.e., the detection of a source depends only on its magnitude (see, e.g., Benítez 2000). The detection probability of our IRAC survey peaks at around $z = 0.8$–1.0. For $z < 0.6$, the detection of sources is dominated by the surveyed volume, and after $z \sim 1.0$, the detection probability decreases exponentially up to $z \sim 4$. About half of our sample lies at $z \gtrsim 0.9$, ~40% at $z > 1$, and ~20% at $z > 1.5$. The bulk of the galaxies in this study (~90%) lie at $z < 2$. This implies that our results for stellar mass functions and densities are very robust up to $z \sim 2$, just where our photometric redshifts are empirically well tested. Beyond that point, we still include ~3000 galaxies, enough to obtain statistically meaningful results (although systematic errors such as redshift outliers will also contribute more to the errors above $z = 2$).

The statistics for the I-band selected sample are very similar to those for the IRAC sample: the average distribution peaks at around $z = 0.7$, and then decays exponentially, enclosing about 50% of the sources below $z = 0.9$, 80% at $z < 1.5$, and 10% at $z > 2.0$. Figure 1 shows that most of the galaxies included in
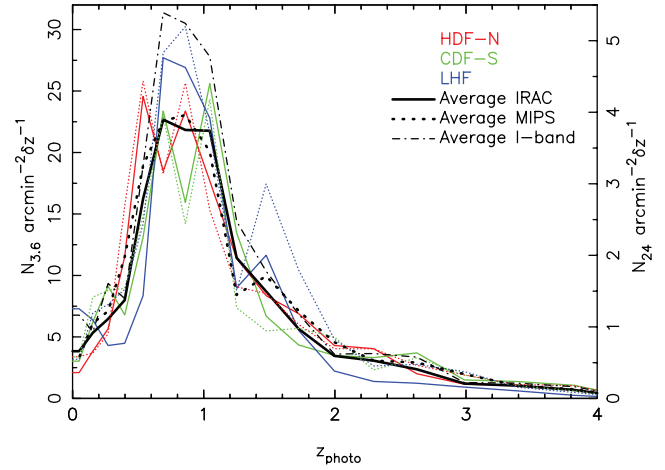

FIG. 1.—Redshift distribution of our IRAC, MIPS, and I-band selected samples (including all galaxies above the completeness level). For the IRAC and MIPS samples, the three fields used in this paper are plotted with different colors, and the average number densities are plotted in black. Solid lines show the number densities for the entire IRAC selected sample (scale on the left vertical axis). Dashed lines show the subsample (within the IRAC sample) also detected at 24 μm (scale on the right vertical axis). The dash-dotted line shows the redshift distribution of the I-band selected sample, with the same scale as the IRAC distribution.

the I-band selected sample and missed by IRAC lie at $z \lesssim 1.5$. At higher redshifts, the number densities of the I-band and IRAC samples are almost identical, which is consistent with the fact that more than 90% of the IRAC sources were detected in our deep Subaru I-band images (cf. Appendix A). This means that the I-band mass completeness level is very similar to the IRAC level, except for $z \lesssim 1.5$, where the I-band should help to probe (slightly) lower masses than the IRAC selection (see Fig. 4). We would need optical images deeper than $I \sim 25.5$ to detect less massive systems at high redshift.

Figure 1 also shows the redshift distribution of the IRAC sources detected by MIPS at 24 μm and having $F(24) = 80\ \mu$Jy (*dashed lines*). The redshift distribution is similar to that presented in Pérez-González et al. (2005), but the improvement in the photometric redshift estimations reveals a more pronounced density bump at $z \sim 1.7$ and a weak bump at $z \sim 2.6$. The origin of these bumps can be found in the increase of the detection probability induced by prominent PAH features entering the MIPS 24 μm filter as we move to higher redshifts (see also Caputi et al. 2006). Indeed, a typical PAH spectrum shows an absence of features around $\lambda = 10\ \mu$m, which produces the detection local minimum at $z \sim 1.3$ observed in Figure 1. At $6 \lesssim \lambda \lesssim 10\ \mu$m, there are several PAH features (the most prominent at 5.5 and 7.7 μm) that are responsible for the bumps in the redshift distribution. Note that the final detected density for MIPS sources is a convolution of the real redshift distribution of galaxies (affected by large-scale structure), the detection probability (dependent on the limiting flux of the survey and the spectra of the galaxies), and the photometric redshift uncertainty distribution. These two effects (detection probability and redshift uncertainties) result in blurring out redshift-dependent features, so they are at lower contrast to the overall real distribution.

5. STELLAR MASS FUNCTIONS AND DENSITIES

5.1. *Completeness of the Sample*

Figure 2 shows the distribution of stellar masses of individual galaxies in our IRAC survey as a function of redshift. The solid blue line shows the stellar mass corresponding to a passively
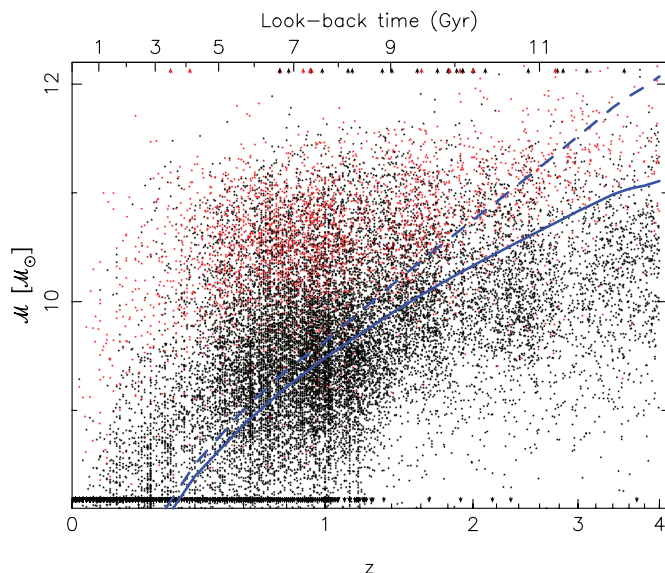
Fig. 2.—Distribution of the stellar masses of all individual galaxies in the IRAC (*all symbols*) and MIPS (*red symbols*) selected samples as a function of redshift (shown with a logarithmic scale in the quantity $1 + z$ in the bottom horizontal axis and the corresponding look-back times in the top axis). The solid blue line shows the stellar mass value at each redshift above which our IRAC survey is 75% complete for passively evolving galaxies. The dashed blue line shows the completeness for highly extincted $[E(B - V) = 1.1]$ bursts. Sources whose stellar mass is beyond the vertical axis scale are plotted with arrows at the source redshift.

evolving galaxy formed in a single instantaneous burst of star formation occurred at $z = \infty$ and having a 3.6 μm flux equal to the 75% completeness level of our IRAC sample. The stellar mass calculated in this way assumes the maximum mass-to-light ratio given by the oldest instantaneously formed stellar population possible at each redshift. Any burst occurring after the primary placed at $z = \infty$ should decrease the observed mass-to-light ratio (unless it presents a high attenuation; see below), thus giving a smaller stellar mass. Therefore, the values given by the solid blue curve in Figure 2 are the minimum stellar masses that a maximally old galaxy with a flux equal to the 3.6 μm 75% completeness level should present, and our survey must be complete (actually, at least 75% complete) against passively evolving galaxies with masses above the continuous curve. As noted by Fontana et al. (2006), high mass-to-light ratios can also be found in galaxies with very extincted bursts. The dashed blue line in Figure 2 shows the completeness level of our survey for instantaneous star-forming bursts extincted by $E(B - V) = 1.1$ mag (as used by Fontana et al. [2006], based on the typical extinction of highly obscured high-redshift galaxies) and following a Calzetti et al. (2000) extinction law.

Note that if the density of galaxies of a given stellar mass at a certain redshift is very small, our surveyed volume may not be large enough to enclose any galaxy of that mass (we would not detect any, although galaxies of that mass might exist in the universe at that redshift). This is the effect seen in Figure 2 at high stellar masses: at $z < 0.2$, our surveyed volume is not large enough to detect galaxies with $M \gtrsim 10^{11.0}\ M_{\odot}$, and we can only detect galaxies with $M \gtrsim 10^{12.0}\ M_{\odot}$ at $z \gtrsim 0.6$. It is also interesting to note that the most massive galaxies with $M \gtrsim 10^{12.0}\ M_{\odot}$ are only found in the regions presenting the highest densities, just where the redshift distribution for individual fields peak (see Fig. 1).

The estimations of the stellar mass functions in the following sections will be carried out for stellar masses above the completeness level (against passively evolving galaxies) shown in Figure 2 (*solid line*), i.e., no completeness correction will be carried out to try to recover the stellar mass function at smaller masses (below the solid blue curve in Fig. 2).

5.2. *Stellar Mass Function Estimation Procedure*

The entire redshift range $0 < z < 4$ was divided into 12 intervals, the size of each bin chosen to have a statistically representative number of galaxies, and taking into account the typical photometric redshift errors. Our goal was to estimate stellar mass functions at each redshift bin. Classical methods to obtain luminosity functions or mass function (see Willmer 1997 for a discussion of them) rely heavily on the use of a flux band on which the selection of the studied sample is based. If the band where the selection is based is far from the band where we want to estimate the luminosity function (or, in the case of estimating stellar mass functions, the magnitude is not directly and easily linked to the stellar mass of each galaxy), significant systematic errors are introduced (see, e.g., Loveday 2000; Ilbert et al. 2004). In our case, our selection is carried out in luminosity at 3.6–4.5 μm, but we want to obtain a stellar mass function, which is linked to that luminosity (but not directly proportional). To solve this problem, we estimated a bivariate luminosity–stellar mass function for each redshift bin. The procedure is identical to that used in Pérez-González et al. (2003a), and accounts for the fact that the selection of the sample is carried out in a certain photometric band, while we eventually want the number density function relative to a different parameter (in our case, the stellar mass). The bivariate luminosity–stellar mass function (BLMF), $\Phi(L, M)$, is defined as the number density of galaxies (in a limited comoving volume given by our surveyed area and the redshift interval considered) with a given luminosity in a certain band and a given stellar mass. This definition is an extension of the bivariate luminosity function (Loveday 2000). The estimation of the BLMF was performed with a stepwise maximum likelihood (SWML) technique (Efstathiou et al. 1988; see also Willmer 1997), extended to consider two independent variables.

To estimate stellar mass functions, we used the IRAC 3.6 μm band as the luminosity variable in the BLMF, given that this is the filter where the selection of the sample was carried out. For the I-band selected sample, we used the I filter as the selection band. Once the BLMF is estimated, if we integrate it through all luminosities, we can estimate the number density of galaxies with a given stellar mass, i.e., the stellar mass function (SMF), $\phi_{SM}(M)$. We only estimated the stellar mass function down to the completeness threshold of the stellar mass discussed in § 5.1.

In the classical SWML method, the errors in the BLMF are estimated from the covariance matrix. In our case, the estimation of the BLMF uncertainties was carried out by combining the SWML technique with a Monte Carlo method to take into account the photometric redshift errors and outliers, as we did in Pérez-González et al. (2005), following the procedure described in Chen et al. (2003). We considered the photometric redshift as a statistical variable whose error comes from the comparison with spectroscopic redshifts. These errors depend on the actual redshift of the galaxy, so we considered different photometric redshift uncertainty distributions for different redshift intervals. We also considered the dependence of the redshift uncertainties on the apparent brightness of the source (more accurate photometry allows better estimations of the photometric redshift), dividing the redshift-dependent distribution of redshift uncertainties into magnitude bins. For $z > 1.5$, where very few spectroscopic redshifts are available to test our photometric redshifts, we only considered one single redshift and magnitude interval. The Monte Carlo method uses the redshift uncertainties based on the comparison with spectroscopy, given that they are more reliable (they

directly test the goodness of the photometric redshifts) than the errors derived from the probability distribution based on the χ^2 minimization, and they include the effect of outliers. The Monte Carlo extension to the SWML method consists of calculating the stellar mass function by randomly varying the redshifts of the whole sample according to the distribution of uncertainties (which are usually non-Gaussian), and calculate the stellar mass function again. After 100 iterations, the average and standard deviations of each point in the stellar mass function are taken as the final results.

The results for the SMF (data points and uncertainties [5]) were fitted with a smooth function using a Schechter (1976) parameterization, to facilitate comparison with similar fits in the literature. Both the IRAC and I-band SMF estimations were used in the fits, down to the IRAC completeness level. For the five bins at highest redshifts, the faint-end slope of the SMF was poorly constrained by our data, so we combined our results with other estimations of the stellar mass functions found in the literature. These estimations are based on the analysis of galaxy samples typically selected at optical wavelengths, which is more effective at probing the low-mass regime of the stellar mass function. We only used literature data points at masses $M > 10^8 \, M_\odot$ at $z < 1.3$ and $M > 10^9 \, M_\odot$ at $z > 1.3$, where the completeness levels of these optically based samples are supposed to be high (based on the sharp turnovers of these SMFs). Note that the completeness of the optically selected samples at masses around $M \sim 10^8$–$10^9 \, M_\odot$ is difficult to estimate (due, for example, to the significant effect of the extinction, and the need of extremely deep data to probe this mass regime) and is not well understood (it is not discussed in the reference papers), so the low-mass slopes at $z \gtrsim 2$ should be taken with caution. The SMF points, errors, and Schechter fits for each redshift bin are shown in Figures 3 and 4 (black filled and open stars for the IRAC and I-band selected samples, respectively). These figures also show other SMF estimations found in the literature (*colored points*; see captions for references). The plots also depict the SMFs and fits for the subsample of galaxies detected simultaneously by IRAC and MIPS at 24 μm (*filled circles*). The data points and Schechter fit parameters are given in Tables 1 and 2, respectively.

5.3. *The Local Stellar Mass Function and Density*

Figure 3 shows our estimations of the local stellar mass function (including sources at $0.0 < z < 0.2$) based on both the IRAC (*filled stars*) and I-band (*open stars*) selected samples. Given that we are surveying a very limited volume in the local universe, we do not detect many sources with $M > 10^{11.0} \, M_\odot$ (this explains the large errors in this mass regime), but our statistics are much better at low masses. Our Schechter fit only refers to the data points above $M > 10^9 \, M_\odot$, where our data are directly comparable with previously published mass functions. Our results are very similar to those published by Cole et al. (2001) and Bell et al. (2003) based on NIR 2MASS data down to the completeness limit of their surveys ($M \sim 10^{9.5} \, M_\odot$). Our deeper data confirm the faint-end slope estimated by Cole et al. (2001) down to even smaller masses, $M \sim 10^{9.0} \, M_\odot$. We also find a steepening of the stellar mass function at $M \lesssim 10^{9.0} \, M_\odot$ (at least for $M \gtrsim 10^{7.9} \, M_\odot$, our completeness level at $z \sim 0$).

By integrating our local SMF, we obtain a value for the local stellar mass density of $\rho_* = 10^{8.75 \pm 0.12} \, M_\odot \, \mathrm{Mpc}^{-3}$, in excellent

[5] Note that the data point at $M = 10^{12.0} \, M_\odot$ in each SMF, which accounts for the very few high-mass sources discussed in § 5.1, presents a very large uncertainty (as it includes very few sources) and has a negligible effect on the Schechter fits.
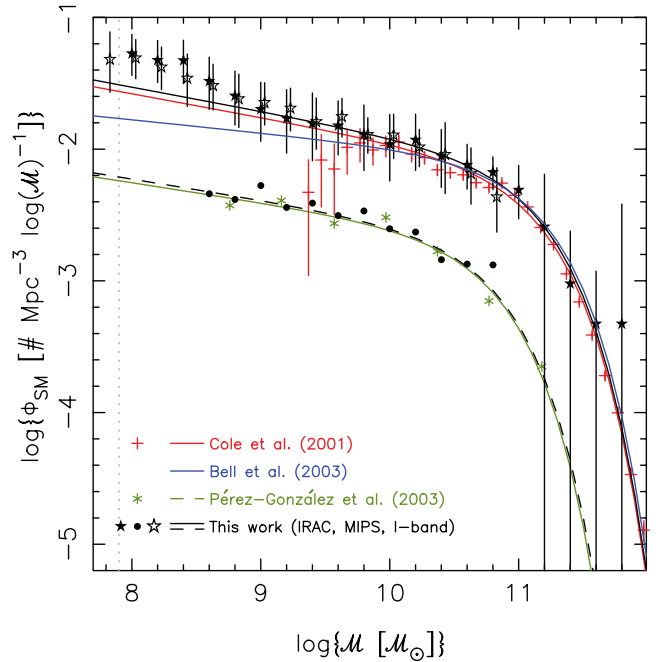

Fig. 3.—Local stellar mass function estimated with the IRAC selected (*filled stars*), I-band selected (*open stars*), and MIPS selected (*filled circles*) samples at $z < 0.2$. For clarity, the I-band data points have been artificially drifted from the original x-position (the same as for the IRAC selected sample), and we do not show the uncertainties for the MIPS data points. The vertical gray dashed line shows the completeness level of our IRAC survey in the local universe. The Schechter fit to the IRAC and I-band data (for masses $M > 10^9 \, M_\odot$) is shown with a solid black line. Our estimation of the local stellar mass function is compared with that estimated by Cole et al. (2001; *red crosses and line*), and by Bell et al. (2003; *blue line*). The best Schechter fit to the data for the MIPS sample (i.e., for local star-forming galaxies) is plotted with a dashed line. This SMF is compared with the one published by Pérez-González et al. (2003a; *green asterisks and line*) for Hα-selected local star-forming galaxies.

agreement with the values found in Salucci & Persic (1999), Cole et al. (2001), and Bell et al. (2003) ($\rho_* = 10^{8.75}$, $10^{8.76}$, and $10^{8.74} \, M_\odot \, \mathrm{Mpc}^{-3}$, respectively). The good agreement of our local stellar mass function and density with previous estimations found in the literature demonstrates that aperture effects in our photometric catalogs are not critical, i.e., they do not affect our results even at low redshifts, where the galaxies present relatively large angular sizes. The steepening of the stellar mass function at $M \lesssim 10^{9.0} \, M_\odot$ has no significant effect on the integrated stellar mass density (justifying the exclusion of these points in the Schechter fit): the galaxies with $10^{7.8} < M < 10^{9.0} \, M_\odot$ contribute less than 2% to the total stellar mass density.

Figure 3 also shows the SMF of the sources detected by MIPS at 24 μm, i.e., the galaxies with active star formation (*filled circles and dashed line fit*). The MIPS results (*data points and fit*) are in excellent agreement with those published by Pérez-González et al. (2003a) for a Hα-selected sample of star-forming galaxies in the local universe. The local stellar mass density locked in star-forming galaxies is $\rho_*^{\mathrm{SF}} = 10^{7.85 \pm 0.07} \, M_\odot \, \mathrm{Mpc}^{-3}$, i.e., 13% $\pm$ 4% of the global stellar mass density in the local universe is found in active star-forming galaxies. Figure 3 also shows that approximately 1 of every 4 galaxies in the local universe with $M \lesssim 10^{10.5} \, M_\odot$ is forming stars currently and would be detected in the IR or with a SFR tracer such as the Hα emission. At higher stellar masses, the fraction of star-forming galaxies decreases by more than a factor of 2 (e.g., $\sim$10% of all galaxies with $M = 10^{11.0} \, M_\odot$ are forming stars actively).
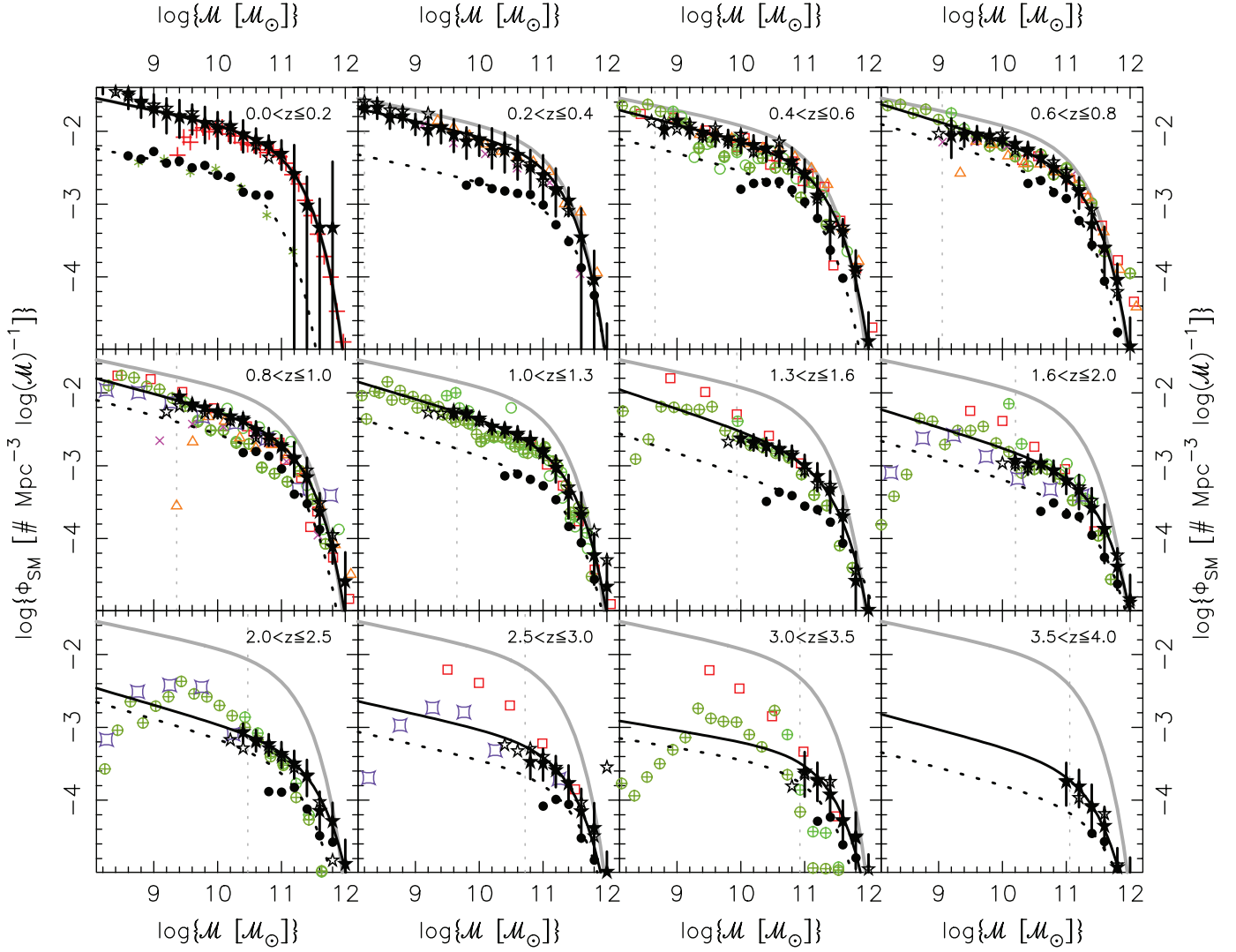
FIG. 4.—Stellar mass functions for 12 redshift intervals from $z = 0$ to 4. Our estimations at each redshift interval are plotted with black filled stars and errors for the IRAC selected sample, and with open black stars for the I-band selected sample (errors for this sample are not plotted, for clarity). Filled circles show the SMF for galaxies detected by MIPS at 24 μm. The SMF data (our estimations and others) are fitted with a Schechter (1976) function (solid black line for the global SMF, and dashed line for the SMF for 24 μm sources). All panels show the local SMF from Cole et al. (2001) with a gray curve. The vertical dotted line shows our 75% completeness limit for the IRAC selected sample (solid curve in Fig. 2). Colored points show estimations from other papers: red crosses come from Cole et al. (2001, C01); orange open triangles from Borch et al. (2006, B06); magenta crosses from Pannella et al. (2006); red squares from Drory et al. (2004, D04) and Drory et al. (2005, D05); green crossed circles from Fontana et al. (2003, FC03; 2004, F04; 2006, F06); and purple squares from Conselice et al. (2005, C05). Green asterisks at $0.0 < z < 0.2$ show the stellar mass function of local star-forming galaxies (Pérez-González et al. 2003a, P03).

5.4. The Evolution of the Stellar Mass Function

Figure 4 presents the global stellar mass functions estimated in the 12 redshift intervals up to $z = 4$. We show the results obtained with the IRAC selected (*filled black stars*), the I-band selected (*open black stars*), and the MIPS selected (*filled circles*) samples. Other estimations found in the literature are also plotted at each redshift interval (normalized to the Salpeter 1955 IMF). We have fitted our SMF data points, and for $z > 1.5$, also the data points from other works below our completeness level to better constrain the slope at lighter masses, to a Schechter function. In the case of the 24 μm galaxies, we assumed the same faint-end slope estimated for the global SMF (based on the IRAC and I-band samples).

Our estimation of the stellar mass function is consistent (within errors and for the same mass ranges) with previous estimations found in the literature. It is interesting to note that the faint-end slope derived by Drory et al. (2005) at $z > 1.5$ is significantly

larger than that found by other authors (Fontana et al. 2004; Conselice et al. 2005). Our results are in good agreement with Drory's in the stellar mass range probed by both surveys. The possible explanations for the discrepancy at low masses are field-to-field variations, an overestimation of the faint-end slope in Drory et al. (2005) due to the use of the $V_{\max}$ method (see Ilbert et al. 2004), or systematic errors in the determination of the stellar masses. Because of this discrepancy, we did not use these points in our SMF fits. At $z > 2$, we estimate number densities of massive galaxies, which can be up to 0.8 dex higher than those estimated by Fontana et al. (2006). Some of this discrepancy (up to ~20%) may be due to the underdensity observed in CDF-S (see § 5.5).

Our results show that the local density of galaxies (shown with a gray line in all panels) with masses $M \gtrsim 10^{12} M_\odot$ was already reached by the SMF at $z = 2.5$–3.0, i.e., the most massive galaxies were already in place at that redshift (approximately 11 Gyr ago). The mass assembly of galaxies shifts to smaller masses as we move to lower redshifts. By $z \sim 1$, the SMF has reached

TABLE 1

STELLAR MASS FUNCTIONS FOR THE GLOBAL AND STAR-FORMING
POPULATION OF GALAXIES

Redshift Range	$\log(M)$ $(M_\odot)$	$\log(\phi_{\mathrm{IRAC}})$[a]	$\log(\phi_{\mathrm{I-band}})$[a]	$\log(\phi_{\mathrm{MIPS}})$[a]
$0.0 < z < 0.2$	8.0	$-1.275^{+0.147}_{-0.165}$	$-1.308^{+0.140}_{-0.157}$	...
	8.2	$-1.325^{+0.150}_{-0.169}$	$-1.377^{+0.152}_{-0.173}$	...
	8.4	$-1.328^{+0.155}_{-0.175}$	$-1.462^{+0.184}_{-0.215}$	...
	8.6	$-1.485^{+0.183}_{-0.213}$	$-1.518^{+0.162}_{-0.184}$	$-2.339^{+0.053}_{-0.061}$
	8.8	$-1.596^{+0.189}_{-0.221}$	$-1.618^{+0.186}_{-0.218}$	$-2.382^{+0.049}_{-0.055}$
	9.0	$-1.698^{+0.205}_{-0.244}$	$-1.647^{+0.151}_{-0.170}$	$-2.278^{+0.045}_{-0.050}$
	9.2	$-1.767^{+0.219}_{-0.263}$	$-1.690^{+0.152}_{-0.172}$	$-2.442^{+0.062}_{-0.072}$
	9.4	$-1.806^{+0.232}_{-0.283}$	$-1.792^{+0.180}_{-0.209}$	$-2.410^{+0.068}_{-0.080}$
	9.6	$-1.823^{+0.189}_{-0.221}$	$-1.754^{+0.139}_{-0.155}$	$-2.504^{+0.050}_{-0.044}$
	9.8	$-1.890^{+0.225}_{-0.273}$	$-1.890^{+0.127}_{-0.141}$	$-2.469^{+0.054}_{-0.062}$

NOTE.—Table 1 is published in its entirety in the electronic edition of the *Astrophysical Journal*. A portion is shown here for guidance regarding its form and content.

[a] In units of $\mathrm{Mpc}^{-3}\,(\log M)^{-1}$.

nearly the local density for galaxies with $M \gtrsim 10^{11.8}\ M_\odot$. At $z < 1$, the star formation in the universe occurs mainly in galaxies with $M \lesssim 10^{11.5}\ M_\odot$. It is also interesting to note the significant evolution (approximately a factor of 0.2 dex or 60%, as shown by our data, and also confirmed by the results of Pannella et al. 2006 and Borch et al. 2006) of the SMF between $z \sim 0.4$ and $z = 0$ (i.e., a period of 4 Gyr) for stellar masses $10^9 \lesssim M \lesssim 10^{11}\ M_\odot$. We comment more on this recent evolution in § 5.5.

Figure 4 also shows that the slope of the SMF at low masses remains approximately constant up to at least $z \sim 2$, at a value $\alpha = -1.2 \pm 0.1$ (consistent with the models in Nagamine et al. 2005b). Only at very low masses ($M \lesssim 10^{9.0}\ M_\odot$ at $z < 1$ and $M \lesssim 10^{10.0}\ M_\odot$ at higher redshifts) does the SMF seem to become steeper (based on our results and those from other surveys), but this steepening has a minor effect on the global stellar mass density.

5.5. *The Evolution of the Cosmic Stellar Mass Density*

The SMFs were integrated for all masses above the completeness level to obtain the observed cosmic comoving stellar mass density. We also integrated the Schechter fits to estimate an
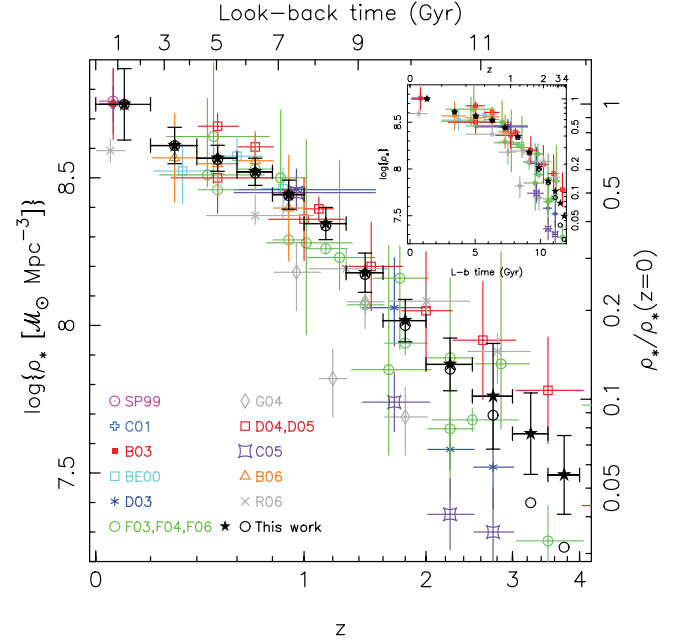

FIG. 5.—Evolution of the stellar mass density of the universe as function of redshift (shown with a logarithmic scale in the quantity $1 + z$ in the bottom horizontal axis and the corresponding look-back times in the top axis). Our estimations are plotted with black filled stars (based on the integration of the stellar mass functions with a Schechter parameterization) and open circles (observed values down to the completeness level). Colored points and error bars show other estimations found in the literature. To the references mentioned in the caption of Fig. 4, we also add estimations from Salucci & Persic (1999, SP99), Brinchmann & Ellis (2000, BE00), Bell et al. (2003, B03), Dickinson et al. (2003b, D03), Glazebrook et al. (2004, G04), and Rudnick et al. (2006, R06). The inset shows the same evolution of the stellar mass density of the universe, but this time with a linear scale in look-back time in the horizontal axis.

extrapolated value of the cosmic stellar mass density at each redshift interval. In Figure 5 we present these results, comparing them with other estimations of the stellar mass density available in the literature (see the captions of Figs. 4 and 5 for references). Note that the observed density values are very similar to the extrapolated ones up to $z \sim 2$, i.e., our survey is detecting most of the galaxies that dominate the global stellar mass density at $z < 2$. We calculate field-to-field variations of the stellar mass

TABLE 2

RESULTS OF THE SCHECHTER (1976) FITS (INCLUDING STELLAR MASS DENSITIES) TO THE GLOBAL AND STAR-FORMING STELLAR MASS FUNCTIONS

REDSHIFT RANGE	GLOBAL					STAR-FORMING				
	α	$\log(M^*)$[a]	$\log(\phi^*)$[b]	$\log(\rho_*)$[c]	$\log(\rho_*^{\mathrm{obs}})$[c]	α_{SF}	$\log(M_{\mathrm{SF}}^*)$[a]	$\log(\phi_{\mathrm{SF}}^*)$[b]	$\log(\rho_*^{\mathrm{SF}})$[c]	$\log(\rho_*^{\mathrm{obs}})$[c]
$0.0 < z \leq 0.2$	-1.18 ± 0.12	11.16 ± 0.25	-2.47 ± 0.22	8.75 ± 0.12	8.75	-1.16 ± 0.12	10.84 ± 0.17	-3.04 ± 0.16	7.85 ± 0.07	7.85
$0.2 < z \leq 0.4$	-1.19 ± 0.08	11.20 ± 0.10	-2.65 ± 0.15	8.61 ± 0.06	8.61	-1.19 ± 0.08	11.33 ± 0.09	-3.30 ± 0.06	8.09 ± 0.05	8.07
$0.4 < z \leq 0.6$	-1.22 ± 0.07	11.26 ± 0.11	-2.76 ± 0.13	8.57 ± 0.04	8.56	-1.22 ± 0.07	11.18 ± 0.06	-3.14 ± 0.05	8.11 ± 0.04	8.07
$0.6 < z \leq 0.8$	-1.26 ± 0.08	11.25 ± 0.08	-2.82 ± 0.12	8.52 ± 0.05	8.52	-1.26 ± 0.08	11.16 ± 0.11	-3.07 ± 0.09	8.18 ± 0.04	8.04
$0.8 < z \leq 1.0$	-1.23 ± 0.09	11.27 ± 0.09	-2.91 ± 0.14	8.44 ± 0.05	8.44	-1.23 ± 0.09	11.20 ± 0.09	-3.19 ± 0.08	8.10 ± 0.04	7.95
$1.0 < z \leq 1.3$	-1.26 ± 0.04	11.31 ± 0.11	-3.06 ± 0.11	8.35 ± 0.05	8.34	-1.26 ± 0.04	11.35 ± 0.05	-3.57 ± 0.06	7.87 ± 0.03	7.75
$1.3 < z \leq 1.6$	-1.29 ± 0.08	11.34 ± 0.10	-3.27 ± 0.18	8.18 ± 0.07	8.17	-1.29 ± 0.08	11.62 ± 0.16	-3.96 ± 0.09	7.77 ± 0.08	7.61
$1.6 < z \leq 2.0$	-1.27 ± 0.11	11.40 ± 0.18	-3.49 ± 0.22	8.00 ± 0.07	8.00	-1.27 ± 0.11	11.45 ± 0.05	-3.93 ± 0.08	7.62 ± 0.04	7.49
$2.0 < z \leq 2.5$	-1.26 ± 0.08	11.46 ± 0.15	-3.69 ± 0.22	7.87 ± 0.09	7.85	-1.26 ± 0.08	11.26 ± 0.10	-3.83 ± 0.16	7.52 ± 0.07	7.29
$2.5 < z \leq 3.0$	-1.20 ± 0.27	11.34 ± 0.39	-3.64 ± 0.43	7.76 ± 0.18	7.70	-1.20 ± 0.27	11.42 ± 0.07	-4.08 ± 0.11	7.40 ± 0.06	7.21
$3.0 < z \leq 3.5$	-1.14 ± 0.21	11.33 ± 0.31	-3.74 ± 0.43	7.63 ± 0.14	7.40	-1.14 ± 0.21	11.26 ± 0.26	-3.97 ± 0.36	7.33 ± 0.17	7.01
$3.5 < z \leq 4.0$	-1.23 ± 0.05	11.36 ± 0.17	-3.94 ± 0.25	7.49 ± 0.13	7.25	-1.23 ± 0.05	11.53 ± 0.10	-4.51 ± 0.15	7.10 ± 0.07	6.86

[a] In units of $M_\odot$.
[b] In units of $\mathrm{Mpc}^{-3}\,(\log M)^{-1}$.
[c] In units of $M_\odot\,\mathrm{Mpc}^{-3}$.

density of the order of 30%–40% (depending on the redshift) with respect to the average density. For example, the stellar mass density locked in galaxies with $M > 10^{11}\ M_\odot$ at $z > 2$ is 15%–20% lower in CDF-S than the average of the three fields, a slightly lower underdensity than that observed by van Dokkum et al. (2006) comparing three $\sim$100 arcmin^2 fields (they calculate a 40% difference of the CDF-S with the average).

Figure 5 shows that there is a relatively large increase (by a factor of $\sim$1.4) in the stellar mass density of the universe in the last 4 Gyr (from $z \sim 0.4$ to $z = 0$). This large difference could be due to an overestimation of the local stellar mass density (suggested by, for example, Fontana et al. 2004) or an underestimation of the density at $z \sim 0.3$ (for example, if low-mass objects below our detection limit have a nonnegligible contribution to the stellar mass density at this redshift). However, all the estimations of the local density are very similar (differences of less than 5% between our value and those found by Salucci & Persic 1999, Cole et al. 2001, and Bell et al. 2003; even higher values are found by Fukugita et al. 1998, Kochanek et al. 2001, and Glazebrook et al. 2003), and the same occurs for the different estimations at $0.2 < z < 0.4$ (Brinchmann & Ellis 2000; Borch et al. 2006). As we discussed in § 5.4, this significant recent evolution of the stellar mass density is mainly due to a $\sim$60% increase in the number density of galaxies with $10^9 \lesssim M \lesssim 10^{11}\ M_\odot$. Assuming an average value of the cosmic SFR density of approximately $0.03\ M_\odot\ \mathrm{yr}^{-1}$ at $0.0 < z < 0.4$ (Hopkins & Beacom 2006; see also Tresse et al. 2007 and Fig. 7), and a 28% gas recycle factor (see § 7.1 for details), we calculate that the stellar mass density of the universe has grown by $10^{8.0 \pm 0.1}\ M_\odot\ \mathrm{Mpc}^{-3}$ from $z = 0.4$ to $z = 0.0$ (in $\sim$4.3 Gyr) by just star formation. This is $55\% \pm 10\%$ of the stellar mass density change at $z < 0.4$. Therefore, the remaining change in stellar mass density ($\sim 10^{7.9 \pm 0.1}\ M_\odot\ \mathrm{Mpc}^{-3}$) must have occurred by either accretion of small satellite galaxies or major mergers between gas-depleted galaxies (i.e., mergers accompanied by very little star formation), as also suggested by Tresse et al. (2007). In addition, given that both in the local universe and at $0.2 < z < 0.4$ the SMFs steepen at low stellar masses ($M \lesssim 10^{9.0}\ M_\odot$), the minor merger possibility (accretion of $M \lesssim 10^{9.0}\ M_\odot$ galaxies producing very few or even no new stars at all) seems to be favored, to the detriment of the existence of major mergers.

The evolution in the previous 3–4 Gyr (between $z \sim 1.0$ and $z \sim 0.4$) was slightly slower. About 25% of the local stellar mass density was assembled in that period, adding up a total decrease of about 50% in the stellar mass density from $z = 0$ to $z = 1$.

At $z \sim 1.0$ (8 Gyr ago), the evolution of the stellar mass density of the universe becomes faster (approximately a factor of 2), just when the cosmic SFR density reaches a maximum (see, e.g., Pérez-González et al. 2005) and the galaxies with $M \gtrsim 10^{10.5}\ M_\odot$ dominate the production of stars in the universe. The rate at which the universe is creating stars stays at approximately a constant level or decays very slowly from $z \sim 1$ up to at least $z \sim 2$ (10 Gyr ago). Between $z \sim 1$ and $z \sim 2$, the density of galaxies with $M \gtrsim 10^{10.5}\ M_\odot$ decreases significantly (by a factor of 3–4). This population of galaxies, evolving rapidly at $1 < z < 2$ (in about 2 Gyr), seems to be dominated by early-type objects (see, e.g., Abraham et al. 2007).

Beyond $z \sim 2$, the errors in the stellar mass density estimates and the differences between the observed and extrapolated values become increasingly larger. We find that the rate at which stars are being formed remains constant or even increases slightly, while the giant galaxies with $M \sim 10^{12.0}\ M_\odot$ are finishing the assembly of most of their stellar mass.
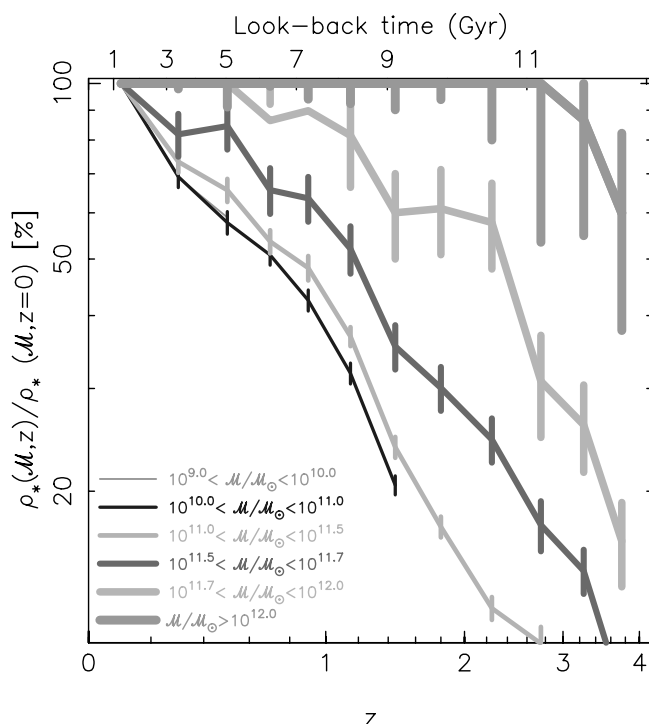

Fig. 6.—Fraction of the local stellar mass density already assembled at a given redshift for several mass intervals (wider lines referring to more massive systems). Only results for masses above our 75% completeness level at each redshift are shown. [*See the electronic edition of the Journal for a color version of this figure.*]

These different steps in the assembly of the cosmic stellar mass density depicted in Figure 5 are consistent with the latest results on the evolution of the observed UV luminosity density of the universe (Tresse et al. 2007) and the evolution of the SFR density (Pérez-González et al. 2005; Hopkins & Beacom 2006) up to $z \sim 5$. The luminosity density presents a maximum at around $z = 1.2$, with a value approximately 6 times larger than the local UV luminosity density. At $z > 1.2$, the luminosity and SFR density evolution is consistent with a constant. Our results are also consistent with the hydrodynamical models of Nagamine et al. (2006), which predict that $\sim$60% of the present stellar mass density was already formed by $z = 1$. However, the discrepancy is significant at $z > 1$, where these models predict a larger stellar mass density than any observation (i.e., they predict a quicker formation of the most massive galaxies). The semianalytic models of Cole et al. (2000) match our results better at $z = 3$–4, where they predict a stellar mass density of about 10% the present value, but they fail to reproduce the evolution at low redshift.

5.6. Quantifying "Downsizing"

The preceding discussion of the evolution of the cosmic stellar mass density is clearly consistent with a "downsizing" scenario for galaxy formation. We quantify some properties of this downsizing theory in Figure 6, were we plot the fraction of the total local stellar mass density already assembled in galaxies of a given stellar mass at each redshift. This figure shows that the most massive systems ($M \gtrsim 10^{12.0}\ M_\odot$; *widest orange solid line*) formed first (they assembled more than 80% of their total stellar mass before $z = 3$) and very rapidly (about 40% of their mass was assembled in 1 Gyr between $z = 4$ and $z = 3$). Systems with masses $10^{11.7} < M < 10^{12.0}\ M_\odot$ assembled their stellar mass more slowly: from $z \sim 4$ to $z \sim 2.5$ (1.5 Gyr), they assembled around

TABLE 3
THE IRAC SAMPLE: COMPARISON WITH OTHER SURVEYS

| | NUMBER OF SOURCES/MIPS DETECTIONS | | | | | | | | NUMBER OF SOURCES | | | |
| | | LBG[b] | | | | | BzK[a] | | LBG[b] | DRG[a] | BzK[a] | Just |
REDSHIFT	IRAC[a]	*GALEX*	BM	BX	"Classic"	DRG[a]	PE	SF	DRG[a]	BzK[a]	LBG[b]	IRAC[a,c]
(0.0, 0.2]	1473/242	0/0	81/11	510/94	2/0	9/4	0/0	468/62	3	9	243	655
(0.2, 0.4]	1745/375	0/0	121/10	183/30	5/0	8/1	0/0	318/54	1	8	134	1252
(0.4, 0.6]	2473/660	0/0	26/1	6/1	9/1	37/4	1/0	303/39	1	32	29	2152
(0.6, 0.8]	3953/979	0/0	55/2	6/0	1/0	38/9	2/1	403/55	1	27	39	3514
(0.8, 1.0]	4226/1065	300/117	273/43	12/2	0/0	78/28	2/0	508/109	7	46	192	3314
(1.0, 1.3]	4140/1012	189/66	1100/189	117/25	1/1	118/48	21/5	1060/130	13	87	540	2233
(1.3, 1.6]	2040/619	0/0	817/213	141/48	5/2	61/26	105/32	1458/439	2	58	804	315
(1.6, 2.0]	1640/532	0/0	414/105	412/129	24/8	55/18	104/33	1417/468	8	55	821	90
(2.0, 2.5]	1404/439	0/0	144/39	551/154	95/29	231/109	49/17	1274/406	43	230	762	52
(2.5, 3.0]	882/264	0/0	4/0	135/31	278/82	253/127	23/15	677/197	59	234	322	68
(3.0, 3.5]	558/162	0/0	0/0	1/1	365/85	171/93	15/10	294/104	49	144	194	52
(3.5, 4.0]	529/95	0/0	0/0	4/0	276/36	165/59	33/20	115/23	40	102	65	117

[a] Any magnitude.
[b] Magnitude limited to $R < 25.5$.
[c] IRAC sources not recovered by any other selection criteria (i.e., they are not LBGs, DRGs, or BzK galaxies).

50% of their stars, and then evolved more slowly to reach the local density at low redshift. Less massive galaxies assembled their mass at even a slower speed, reaching the local density at very recent epochs. Again, this plot shows the rapid recent evolution of the galaxies with masses $M \sim 10^{10.5}\ M_\odot$, which assembled $\sim$30% of their mass in the last 3 Gyr.

Our results are consistent with the stellar population models assumed by Brown et al. (2007) for the most luminous (and probably most massive) red galaxies. According to that paper, red massive galaxies start forming at an early epoch, at $z = 4$, following an exponential SF law with a short $\tau = 0.6$ Gyr. Jimenez et al. (2007) find that the most massive early-type galaxies in the local universe formed at $z > 2.5$ and experienced a very rapid chemical enrichment, lasting 1–2 Gyr. Van der Wel et al. (2005) also find signs of the formation of massive ($M > 2 \times 10^{11}\ M_\odot$, according to these authors) early-type galaxies at $z \gtrsim 2$, while less massive systems present lower formation redshifts ($1 < z < 2$). The analysis of optical spectra for spheroidal and bulge-dominated galaxies at $0.2 < z < 1.2$ by Treu et al. (2005) also reveals that most of the mass (99%) in systems with $M > 10^{11.5}\ M_\odot$ formed at $z > 2$, while most recent bursts (at $z \sim 1.2$) can account for 20%–40% of the total stellar mass of galaxies with $M < 10^{11.0}\ M_\odot$. Glazebrook et al. (2004) estimates that 38% $\pm$ 18% of the stellar mass density in galaxies with $M > 10^{10.8}\ M_\odot$ were already in place at $z = 1$, consistent with our value of $\sim$45%. At $z = 1.8$, Glazebrook et al. (2004) obtain 16% $\pm$ 6%, also in agreement with our own estimation of $\sim$21%.

If we consider a high value of the fraction of the stellar mass density already assembled at a given redshift, above which the star formation in a galaxy should be relatively low, e.g., 70%, Figure 6 shows that galaxies with $M \sim 10^{10.5}\ M_\odot$ reached that level at $z \sim 0.2$, systems with $M \sim 10^{11.25}\ M_\odot$ at $z \sim 0.4$, and galaxies with $M \sim 10^{11.75}\ M_\odot$ around $z \sim 0.7$. These numbers are roughly consistent with the $(1 + z)^{3.5}$ evolution estimated by Bundy et al. (2006) for the quenching stellar mass (M_Q), a mass limit above which the star formation appears to be suppressed.

According to Figure 6, 50% of the stars in galaxies with $M > 10^{11.0}\ M_\odot$ were already in place at $z \sim 0.9$. This compares well with the prediction from the models in De Lucia et al. (2006), which establish that half of the stars in objects of this mass are

assembled into single objects at $z \sim 0.8$. However, these models also predict that most of these stars were already formed at $z \sim 2.5$, but were placed in several objects that would coalesce into a single object later in a hierarchical way. Our results favor a dual scenario, in which the most massive systems with $M \gtrsim 10^{12.0}\ M_\odot$ formed most of their stars at $z > 2.5$ and assembled very rapidly in a way closer to a monolithic collapse than to a hierarchical coalescence. At the same time, less massive systems ($10^{11.0} \gtrsim M \gtrsim 10^{12.0}\ M_\odot$) could have formed their stars later and/or assembled half of their mass from several progenitors (where stars were already formed at $z \sim 2.5$) in the time interval between $z \sim 2.5$ and $z \sim 1$ (about 4 Gyr), and most of their mass (80%) not before $z \sim 0.5$. To confirm this scenario, it would be necessary to probe the stellar mass function at low masses (for objects that would act as building blocks for the galaxies with $M \gtrsim 10^{11.0}\ M_\odot$), but the scatter of the currently available SMF estimations at low masses in this redshift range is too large to obtain robust results (possibly due to cosmic variance effects). Indeed, our estimations of the cosmic stellar mass density at $z > 3$ are affected by the large uncertainties at masses below $10^{11}\ M_\odot$ (this explains the large difference between the observed and extrapolated values of the density at $z > 3$). The dual galaxy formation scenario (quasi-monolithic and rapid collapse of the most massive galaxies which cease to form stars at a certain epoch, and hierarchical collapse for less massive systems) has been reproduced by other models where AGNs are supposed to quench the star formation in very massive halos (see, e.g., Croton et al. 2006; Bower et al. 2006).

6. THE NATURE OF THE IRAC SAMPLE: COMPARISON WITH OTHER SURVEYS

In this section, we discuss the main properties of the sources in our IRAC sample, comparing them with the populations of galaxies detected with different selection techniques by other surveys. The results discussed in this section are summarized in Tables 3 and 4.

Based on the observed photometric data points and the SED fit for each galaxy in our sample, we estimated synthetic observed magnitudes in nine bands (FUV, NUV, U_n, B, $\mathcal{G}$, $\mathcal{R}$, z, J, and K_s) in order to test which of our galaxies would qualify as Lyman

TABLE 4
The IRAC Sample: Stellar Mass Statistics and Contribution to the Stellar Mass Density

	All	LBG				DRG				BzK			
		Stellar Masses[a] and Percentage of Total Stellar Mass Density											
Redshift	IRAC	Any Magnitude		R < 25.5		Any Magnitude		K < 22.9		Any Magnitude		K < 22.9	
(0.0, 0.2]	$7.4^{8.3}_{6.5}$	$7.2^{8.1}_{6.2}$	12%	$7.4^{8.2}_{6.5}$	12%	$7.7^{8.5}_{7.6}$	0%	$8.3^{8.5}_{7.8}$	0%	$6.6^{7.3}_{5.8}$	1%	$7.3^{8.0}_{6.6}$	1%
(0.2, 0.4]	$8.8^{9.5}_{8.2}$	$8.1^{8.8}_{7.5}$	6%	$8.2^{8.9}_{7.6}$	6%	$8.5^{9.2}_{8.3}$	0%	$8.9^{9.4}_{8.4}$	0%	$7.9^{8.6}_{8.5}$	4%	$8.7^{9.1}_{8.0}$	3%
(0.4, 0.6]	$9.6^{10.1}_{9.1}$	$9.0^{9.3}_{8.7}$	0%	$9.1^{9.3}_{8.8}$	0%	$8.6^{9.7}_{8.4}$	1%	$9.5^{10.0}_{9.7}$	1%	$9.0^{9.3}_{8.4}$	3%	$9.4^{9.7}_{9.5}$	2%
(0.6, 0.8]	$9.7^{10.2}_{9.2}$	$9.1^{9.5}_{8.8}$	5%	$9.2^{9.5}_{8.8}$	5%	$9.7^{10.2}_{8.8}$	1%	$10.1^{10.2}_{9.7}$	0%	$9.1^{9.5}_{8.4}$	6%	$9.7^{10.0}_{9.3}$	6%
(0.8, 1.0]	$9.8^{10.3}_{9.3}$	$9.7^{10.1}_{9.2}$	18%	$9.7^{10.1}_{9.3}$	18%	$9.9^{10.4}_{9.2}$	1%	$10.2^{10.5}_{9.8}$	1%	$9.4^{9.9}_{8.7}$	8%	$10.0^{10.3}_{9.5}$	7%
(1.0, 1.3]	$9.8^{10.4}_{9.4}$	$9.5^{9.9}_{9.1}$	22%	$9.6^{10.0}_{9.2}$	21%	$10.1^{10.6}_{9.5}$	8%	$10.4^{10.7}_{9.9}$	8%	$9.6^{10.1}_{9.1}$	19%	$10.2^{10.5}_{9.8}$	17%
(1.3, 1.6]	$10.2^{10.7}_{9.8}$	$9.9^{10.2}_{9.6}$	24%	$10.0^{10.3}_{9.6}$	23%	$10.7^{11.3}_{10.4}$	7%	$11.0^{11.3}_{10.7}$	7%	$10.2^{10.6}_{9.8}$	72%	$10.6^{10.9}_{10.3}$	67%
(1.6, 2.0]	$10.3^{10.7}_{10.0}$	$10.1^{10.5}_{9.8}$	44%	$10.2^{10.5}_{9.8}$	42%	$10.7^{11.0}_{10.4}$	7%	$10.9^{11.1}_{10.8}$	6%	$10.3^{10.7}_{9.9}$	93%	$10.7^{11.2}_{10.4}$	87%
(2.0, 2.5]	$10.4^{10.9}_{10.0}$	$10.2^{10.6}_{10.0}$	52%	$10.2^{10.6}_{10.0}$	45%	$11.0^{11.2}_{10.7}$	34%	$11.1^{11.4}_{10.9}$	31%	$10.4^{10.9}_{10.0}$	97%	$10.9^{11.2}_{10.6}$	83%
(2.5, 3.0]	$10.4^{10.9}_{10.0}$	$10.3^{10.8}_{9.9}$	45%	$10.3^{10.7}_{9.9}$	34%	$11.0^{11.3}_{10.8}$	63%	$11.2^{11.4}_{11.0}$	53%	$10.5^{11.0}_{10.1}$	87%	$11.0^{11.3}_{10.8}$	69%
(3.0, 3.5]	$10.5^{10.9}_{10.0}$	$10.4^{10.9}_{9.8}$	62%	$10.3^{10.8}_{9.8}$	44%	$11.1^{11.4}_{10.8}$	73%	$11.4^{11.6}_{11.2}$	62%	$10.7^{11.2}_{10.3}$	81%	$11.3^{11.6}_{11.1}$	64%
(3.5, 4.0]	$10.5^{10.9}_{10.0}$	$10.4^{10.8}_{10.0}$	45%	$10.4^{10.7}_{9.9}$	34%	$11.0^{11.3}_{10.7}$	69%	$11.3^{11.5}_{11.1}$	50%	$10.9^{11.3}_{10.6}$	56%	$11.4^{11.6}_{11.1}$	39%

[a] Logarithms of the median and quartiles of the distribution of stellar masses in units of $[M_\odot]$.

break galaxies (LBGs) at $z = 1.5$–2.5 (LBG-BM and LBG-BX galaxies in Steidel et al. 2004), at $z \sim 3$ ("classical" LBGs; Steidel et al. 2003), and at $z \sim 1$ (*GALEX* LBGs; Burgarella et al. 2006), and which of our galaxies would qualify as distant red galaxies (DRGs; Franx et al. 2003; van Dokkum et al. 2003) or *BzK* sources (Daddi et al. 2004). Our analysis is similar to that used by Quadri et al. (2007) and Grazian et al. (2007).

We identified LBGs following Steidel et al. (2003, 2004), who establish the locus of LBGs in a $Un - \mathcal{G}$ versus $\mathcal{G} - \mathcal{R}$ color-color diagram, and adopt the magnitude cut ($R < 25.5$) for their survey. We identified *GALEX* LBGs with an analog procedure, but this time using a color criteria based on *GALEX* UV photo-metric bands (see Burgarella et al. 2006). Following Franx et al. (2003), we defined DRGs as the galaxies presenting a color $J - K_s > 1.37$ [corresponding to $(J - K_s)_{\rm Vega} > 2.3$]. Finally, we identified star-forming *BzK* galaxies (*BzK*-SF) and passively evolving *BzK* galaxies (*BzK*-PE) using equations (2) and (3) from Daddi et al. (2004). In our IRAC selected sample, we identified 6656 sources as LBGs with $R < 25.5$ (summing up all types), 763 sources as DRGs with $K < 22.9$, and 2426 as *BzK* sources with $K < 22.9$ and $z > 1.4$ (summing up the two types).

The average surface density of LBGs (including all subtypes) with $R < 25.5$ detected by our IRAC survey is 10.0 LBGs arcmin^{-2}. We detect 0.7 LBGs arcmin^{-2} with the *GALEX* bands and NUV < 25.0, a higher density than the one given by Burgarella et al. (2006, 0.3 arcmin^{-2}), but closer to the density given in Burgarella et al. (2007, 1.0 arcmin^{-2}). We find 4.6 LBG-BMs arcmin^{-2} (5.3 LBG-BMs arcmin^{-2} without any optical magnitude cut), 3.1 LBG-BXs arcmin^{-2} (3.6 LBG-BXs arcmin^{-2} without any optical magni-tude cut), and 1.6 "classical" LBGs arcmin^{-2} (2.0 classical LBGs arcmin^{-2} at any R magnitude), very similar values to those found in Steidel et al. (2004, 5.3 LBG-BMs arcmin^{-2} and 3.6 LBG-BXs arcmin^{-2}) and Steidel et al. (2003, 1.7 classical LBGs arcmin^{-2}. Adelberger et al. (2004) and Grazian et al. (2007) also find very similar surface densities for the three types of LBGs at $z > 1$. The median magnitudes for the LBG subsample are $R = 24.6$ and $K = 23.1$, a very faint NIR magnitude only reachable by the deepest ground-based or IRAC surveys. The average photomet-ric redshifts for the LBGs in our sample are consistent with the literature, as discussed in Appendix B, jointly with the results for the other populations of high-redshift galaxies.

The average surface density of DRGs in our IRAC survey is 1.8 DRGs arcmin^{-2} (1.1 DRGs arcmin^{-2} for sources with $K < 22.9$), a value in between the densities quoted by Franx et al. (2003, 3.0 DRGs arcmin^{-2}), Förster Schreiber et al. (2004, 1.0–1.6 DRGs arcmin^{-2}), and Papovich et al. (2006, 0.8 DRGs arcmin^{-2}). The median magnitudes for the DRG subsample are $R = 25.7$ (a very faint optical magnitude beyond the reach of most UV/optical surveys) and $K = 22.6$.

The average surface density of *BzK* galaxies at $z > 1.4$ down to $K = 21.9$ is 1.3 *BzK*s arcmin^{-2}, divided into 0.2 *BzK*-PE arcmin^{-2} and 1.1 *BzK*-SF arcmin^{-2}. This is consistent with the densities given in Daddi et al. (2004, 0.22 *BzK*-PE arcmin^{-2} and 0.91 *BzK*-SF arcmin^{-2}) for the same brightness limit. At fainter magnitudes, $K < 22.9$, we identify 0.4 *BzK*-PE arcmin^{-2} and 3.3 *BzK*-SF arcmin^{-2}, close to the values found by Reddy et al. (2006b, 0.24 *BzK*-PE arcmin^{-2} and 3.1 *BzK*-SF arcmin^{-2}) and Grazian et al. (2007, 0.65 *BzK*-PE arcmin^{-2} and 3.2 *BzK*-SF arcmin^{-2}) for the same magnitude cut. At even fainter K-band magnitudes, the source density of galaxies identified as *BzK* con-tinues to rise (especially the SF subtype) as redshift interlopers become more numerous (up to 40%).

These figures (densities and average redshifts) demonstrate that our IRAC survey constitute an almost complete census of the previously detected galaxies at $1.5 \lesssim z \lesssim 4$, including most of the LBGs, DRGs, and *BzK* sources, the most important pop-ulations of galaxies selected at $z > 1$. Still, some of the IRAC sources are not recovered by any of these selection criteria (even when no magnitude cut is performed for LBGs, DRGs, or *BzK* sources). The numbers of these galaxies recovered only by the deep IRAC observations are given in Table 3.

The LBG population accounts for a negligible fraction (less than 10%) of the entire IRAC sample at $0.4 < z < 1.0$. At $z < 0.4$, $\sim$30% of IRAC galaxies are classified as LBGs (40% at $0.0 < z < 0.2$ and 20% at $0.2 < z < 0.4$), most of them within the LBG-BX subtype, which has a significant fraction of $z < 1$ interlopers at bright apparent magnitudes (see Steidel et al. 2004). LBGs selected with *GALEX* bands are also a minor frac-tion (around 5%) of the total number of IRAC galaxies at $0.8 < z < 1.3$. However, at $z > 1$, other LBG subtypes start to be very numerous and even dominate the IRAC galaxy counts: $\sim$35% of all the sources in our IRAC survey at $1.0 < z < 1.3$ are LBGs

(80% of them LBG-BMs), 50%–60% at $1.3 < z < 3.0$ (with similar contributions from the different subtypes), 65% at $3.0 < z < 3.5$ (all of them classical LBGs), and 50% at $3.5 < z < 4.0$ (all of them classical LBGs). These fractions are slightly higher for LBGs not limited by any R-band magnitude.

The median stellar masses of LBGs range from $10^{9.6}$ to $10^{10.2}$ $M_\odot$ at $1 < z < 2.5$. These values are 0.1–0.2 dex lower than the median stellar masses for the global population of IRAC sources at each redshift interval. For this reason, although their numbers are relatively large (even dominating the number counts), LBGs make a less important contribution to the global stellar mass density. Indeed, at $1.0 < z < 1.6$, they harbor less than 25% of the total stellar mass density.[6] At $1.6 < z < 4.0$, they account for 35%–45% of the total stellar mass density (roughly consistent with the estimations from the models in Nagamine et al. 2005b). These percentages increase by 5%–15% if we consider all LBGs without any R-band cut, then making our estimations consistent with those in Grazian et al. (2007) where they do not apply any magnitude cut.

Around 10% of LBGs are detected by MIPS at 24 μm above the 75% completeness flux level (20% with any flux), especially at $1.6 < z < 2.5$, where MIPS is more efficient at detecting sources due to the pass of the 7.7 μm PAH feature through the filter. At $z > 2.5$, the fraction of MIPS detections is about 10%, consistent with Huang et al. (2005). MIPS detections are more common for the highest mass galaxies: the median stellar mass for 24 μm detected LBGs [$10^{10.9}$ $M_\odot$ at $z \sim 2.5$ and $10^{11.1}$ $M_\odot$ at $z \sim 3.0$ for sources with $F(24) = 80$ μJy] is $\sim$0.8 dex larger than the median for all LBGs. LBGs with MIPS detections account for 10%–20% of the total stellar mass at $z > 1.5$.

In contrast to the previous figures for LBGs, DRGs are less numerous but more massive. DRGs only account for 15% of the sources at $2.0 < z < 2.5$, and $\sim$30% at $2.5 < z < 4.0$. However, their median stellar masses are larger than those of LBGs at each redshift, and even larger than the median for the entire population of IRAC sources. For $1 < z < 2$, their median masses are 0.3–0.5 dex larger than those for the entire IRAC population, and at $z > 2$ they remain $\sim$0.6 dex larger (with a median of $10^{11.0}$ $M_\odot$). This translates to DRGs accounting for 70% of the total stellar mass density at $z > 2.5$, $\sim$35% at $2.0 < z < 2.5$, and less than 10% below $z = 2$. These figures are very similar to those found by Rudnick et al. (2006), that DRGs contribute 30% and 64% to the stellar mass density at $z \sim 2$ and $z = 2.8$, respectively. They are also consistent with the results obtained by Grazian et al. (2007), Marchesini et al. (2007), and van Dokkum et al. (2006). Note that most of the stellar mass density of the universe at $z > 2.5$ would not be detected by optical surveys reaching depths brighter than $R \sim 25.5$. Consistent with Papovich et al. (2006) and Webb et al. (2006), we find that within the DRG population, about 40% are detected by MIPS at 24 μm (up to 50% at $2.0 < z < 3.5$), and these objects have median stellar masses 0.1–0.3 dex larger than the median for all DRGs. DRGs with MIPS detections account for more than 40% of the total stellar mass at $z > 2.5$ (20% at $2.0 < z < 2.5$, and less than 5% at $z < 2.0$).

The BzK criterion is very effective for detecting massive galaxies at $z > 1.5$, even more than the $J - K$ selection of DRGs. Up to 75%–95% of the IRAC sources at $1.3 < z < 2.5$ are recovered by the BzK selection, 80% at $2.5 < z < 3.0$, 55% at $3.0 < z < 3.5$, and 30% beyond $z = 3.5$. If we only consider

BzK galaxies with $K < 22.9$, these percentages decrease by a factor of $\sim$2. Most of the BzK galaxies are classified as star-forming (typically 90%). Median masses for BzK galaxies range from $10^{10.2}$ at $z = 1.5$ to $10^{10.6}$ at $z = 3.0$ and $10^{10.9}$ at $z = 4.0$, 0.1–0.4 dex larger than median stellar masses for the whole IRAC sample. This translates into BzK galaxies tracing a large fraction of the stellar mass density at $z > 1.5$: more than 55%, and up to 97% at $z > 1.3$. Again, if we only consider BzK galaxies with $K < 22.9$, these percentages decrease by 15%–20%. These fractions are comparable to the 94% contribution of BzK sources to the total stellar mass density at $z \sim 1.8$ found by Grazian et al. (2007). Typically, 30% or more BzK galaxies are detected by MIPS at 24 μm, with a predilection for the passively evolving subtype at $z > 2$ ($\sim$60% and $\sim$30% of BzK-PE and BzK-SF galaxies are detected by MIPS). This means that passively evolving BzK galaxies may still harbor significant star formation or obscured AGNs.

Very few galaxies are identified as LBGs and DRGs simultaneously in our IRAC survey: just 5% of all galaxies at $2.0 < z < 3.0$, $\sim$8% at $z > 3$, and less than 1% elsewhere. However, this does not mean that the two selection criteria are completely orthogonal. Indeed, about 20% of the DRGs at $z = 2$–3 and 30% of the DRGs at $z > 3$ qualify as LBGs, and 15% of LBGs at $z > 2.5$ are DRGs. Most of the LBGs that also qualify as DRGs lie in the classical subtype (more than 95% of them), which makes our results also consistent with the fractions found in Grazian et al. (2007), who only discussed BM-BX objects. Note that if we only consider the DRGs brighter than $K = 21.9$, the fraction of LBGs that are also DRGs drops below 5%, in good agreement with the 10% upper limit prediction from the hydrodynamic models of Nagamine et al. (2005a).

The BzK and DRG selection criteria present a large overlap. Around 20%–30% of all IRAC galaxies at $z > 2$ are recovered by both selection techniques, especially by the BzK-SF criterion. Indeed, more than 95% of all DRGs at $1.5 < z < 3.0$ are BzK galaxies, most of them ($\sim$90%) within the star-forming BzK subtype (in agreement with Grazian et al. 2007). DRGs are only a minor contributor to the BzK population at $z < 3$, where less than 35% of BzK sources are DRGs, but this percentage rises to 70% at $z > 3.5$. It is also interesting to mention that 50% of BzK-PE galaxies at $2.0 < z < 2.5$ and all the BzK-PE galaxies at $z > 2.5$ are DRGs.

None of the LBGs lie in the BzK-PE type (as also noted by Grazian et al. 2007), but the BzK-SF type also has a large overlap with the LBG population: more than 95% of BM-BX galaxies up to $z \sim 2$ are recovered in the BzK diagram (consistent with Reddy et al. 2005), and less than 40% in the case of classical LBGs at $z > 3$.

7. LINKING STELLAR MASSES AND STAR FORMATION RATES UP TO $z = 4$

7.1. *The Evolution of the Cosmic Star Formation Rate Density*

The time derivative of the stellar mass density function plotted in Figure 5 can be used to obtain the evolution of the SFR density of the universe, i.e., the well-known Lilly-Madau plot (Lilly et al. 1996; Madau et al. 1996). For each pair of stellar mass density points in Figure 5, we have estimated the SFR density (averaged through the time interval enclosed by the points) necessary to produce the stellar mass density difference between the corresponding redshifts. This SFR density must be corrected upward by some amount to account for the mass loss due to stellar winds and supernova ejecta. For a Salpeter IMF, the correction is 28% (Cole et al. 2001; Dickinson et al. 2003b; Hopkins & Beacom

---

[6] This percentage has been calculated by adding the total stellar masses of LBGs in that redshift interval, and dividing it by the total stellar masses of all galaxies. This must be analogous to dividing the stellar mass densities of both galaxy populations for a fixed volume (that enclosed at the given redshift interval).
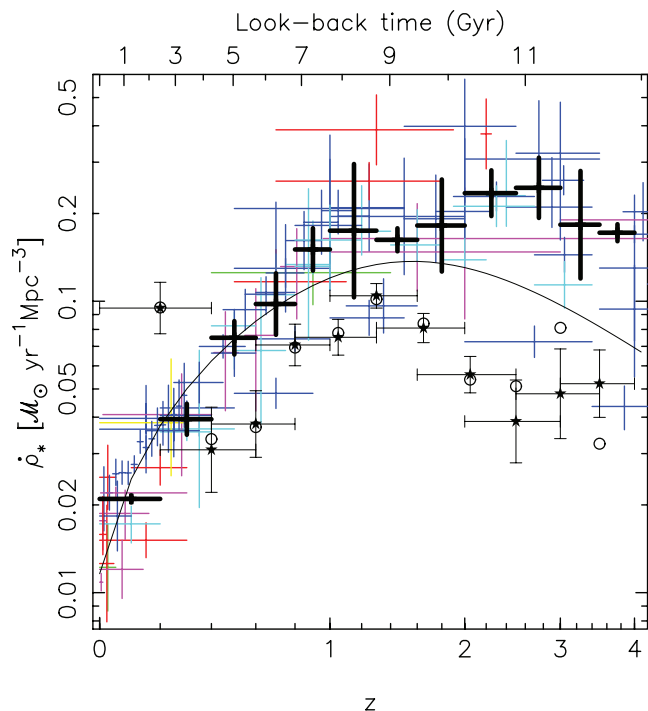
Fig. 7.—Evolution of the comoving SFR density of the universe (Lilly-Madau plot; Lilly et al. 1996; Madau et al. 1996). Filled stars and thin error bars show the SFR density estimations based on the time derivative of the stellar mass density evolution shown in Fig. 5. Open circles show the derivative for the observed values of the stellar mass density. The colored points (shown with error bars) are extracted from different sources in the literature (using different SFR tracers), compiled and normalized to the same cosmology by Hopkins (2004) and Hopkins & Beacom (2006). To this compilation, we have also added the SFR density estimations at $z \sim 2$ and $z \sim 3$ found in Reddy et al. (2007). Red symbols are estimations based on hydrogen emission lines, and green points on [O II] $\lambda 3737$ SFR estimations. UV-based data points are plotted in blue. Cyan estimations are based on mid-IR data. Magenta points are based on submillimeter and radio observations. The yellow point is based on X-ray data. Thick black error bars show weighted averages and standard deviations of the literature data points for the 12 redshift intervals considered for the stellar mass functions in this paper. The black line shows the evolution of the cosmic SFR density as parameterized in Cole et al. (2001).

2006). These SFR density estimations are plotted in Figure 7 with filled black stars (open circles show the average SFR densities derived from the observed stellar mass density values), and compared with other cosmic SFR density estimations (based on direct SFR measurements) found in the literature. Surprisingly, our estimations of the cosmic SFR density are systematically smaller than the previously published results (on average, a factor of ~ 1.7 at $z < 2$ and a factor of 4.5 at higher redshifts, compared to individual estimations). This discrepancy has also been remarked by Rudnick et al. (2006), Hopkins & Beacom (2006), and Borch et al. (2006), who integrate the time evolution of the cosmic SFR density to obtain the evolution of the stellar mass density.

Rudnick et al. (2006) find a factor of 1.6–2.5 offset at $z < 2$ between the measured stellar mass densities and the values derived from the integration of the SFR density evolution published by Cole et al. (2001). At $z > 2$, they find very good agreement. However, the fit of the SFR density evolution published by Cole et al. (2001) gives a factor of 2–3 lower SFR densities than the latest estimations at $z \gtrsim 2$ (see Fig. 7).

Hopkins & Beacom (2006) argue that the difference can be related to a limitation in our understanding of the IMF, given that the direct SFR estimations are sensitive to the high-mass end of

the IMF, while the stellar mass estimations are sensitive to the low-mass end. Indeed, Borch et al. (2006) find good agreement between the SFR and the stellar mass density evolution at $z < 1$ by choosing a Chabrier (2003) IMF, which gives stellar masses similar to a Kroupa et al. (1993) IMF (~ 1.7 times lower than our masses, based on a Salpeter IMF), but with lower SFRs (by a factor of 3). In our case, an offset of $3/1.7 \sim 1.8$ would also make consistent the results of the evolution of the SFR density and stellar mass density up to $z \sim 2$. However, at $z \gtrsim 2$, the same Chabrier (2003) IMF fails to match the SFR and stellar mass densities: using the same Chabrier IMF, a good fit to the stellar mass density evolution gives SFR densities lower than the latest observations by up to a factor of 2–3. A top-heavy IMF (compared to a Chabrier IMF) at high redshifts (i.e., an evolution of the IMF) could make the SFR and stellar mass density evolutions at $z \gtrsim 2$ match. A top-heavy IMF has also been proposed in the galaxy evolution models of Baugh et al. (2005) and Lacey et al. (2007) to explain the number counts of galaxies in the IR and submillimeter spectral ranges (see also, among others, Elmegreen 2004; Nagashima et al. 2005; Silk 2005; Le Delliou et al. 2006; Klessen et al. 2007). Theoretical calculations of formation of stars also predict a top-heavy IMF for starbursts (e.g., Padoan et al. 1997; Larson 1998; Kroupa 2007). Finally, some observational evidence also suggests a top-heavy IMF for certain stellar populations (Franceschini et al. 2001; van Dokkum & van der Marel 2007; Maness et al. 2007).

The discrepancy in Figure 7 could also be solved if the SFRs estimated (with different star formation tracers, mainly the UV, IR, and submillimeter emission) for the massive galaxies at $z \gtrsim 2$ were overestimated due to, for example, the presence of a strong obscured AGN in most of these sources (see Daddi et al. 2007 and references therein), which would imply that a significant fraction of their UV or IR emission arises from the AGN, i.e., it is not linked to star formation.

Finally, the reader should also note the very high SFR density derived for $0.0 < z < 0.4$ from the stellar mass density derivative, directly related to the significant increase in the stellar mass density of the universe in this time period, as discussed in previous sections. Direct SFR density measurements at $z < 0.4$ are a factor of 2–4 smaller, which indicates that the evolution of the stellar mass function at low redshift is not only governed by star formation (but also by mergers), and/or that we may be underestimating the stellar mass density at $z \sim 0.4$ (if there is a numerous population of low-mass galaxies below our detection limit, which can merge together in the last 4 Gyr to increase the density of galaxies with mass $M = 10^9 - 10^{11} M_\odot$) or overestimating the local value. In § 5.5, we estimated a change of the stellar mass density of $10^{7.9 \pm 0.1} M_\odot$ Mpc^{-3} from $z = 0.4$ to $z = 0.0$ due to dry mergers. Since these mergers are affecting galaxies with $M = 10^9 - 10^{11} M_\odot$ and the average number density of these systems is $10^{-2.1}$ Mpc^{-3} log (M) at $0.2 < z < 0.4$, we calculate a mass accretion rate of $\Delta M/M = 0.12 \pm 0.03$ Gyr^{-1} from $z = 0.4$ to $z = 0.0$. This value is in good agreement with the accretion rate of $z = 0.1$ galaxies in the red sequence, estimated by van Dokkum (2005) as 0.09 ± 0.04 Gyr^{-1} (our value is just 30% higher, but consistent within errors); they also calculate that the median mass ratio of the mergers in nearby early-type galaxies is 1:4.

7.2. Specific Star Formation Rates

Figure 8 shows the evolution of the specific SFR (SFR per stellar mass unit) of the universe (gray shaded area), calculated by dividing the average values of the cosmic SFR density (given in Fig. 7) by our stellar mass density estimates (given in Fig. 5).
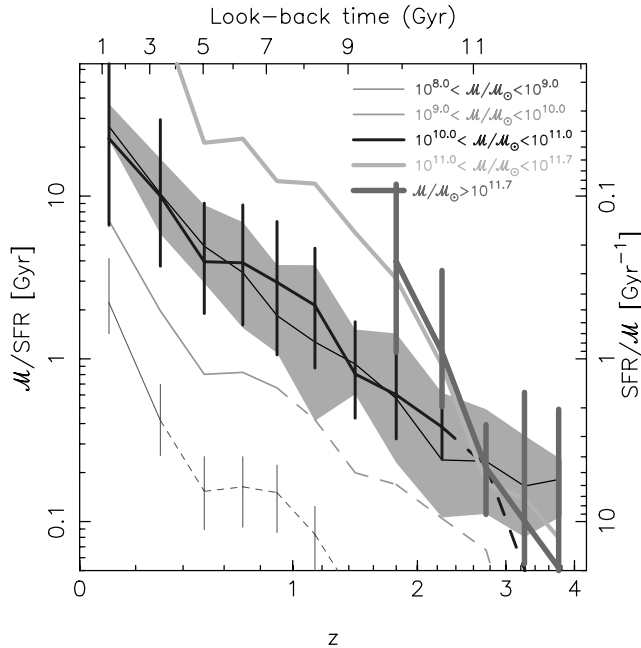
Fig. 8.—Evolution of the cosmic specific SFR. The solid black line shows the evolution obtained from the stellar mass and SFR density estimates plotted in Figs. 5 and 7. The gray-shaded area depicts the typical uncertainties in the calculation of the cosmic specific SFR. Color lines join the median values of the distribution of specific SFRs of our IRAC sample for several mass intervals (excluding all X-ray-detected sources), while vertical error bars show the quartiles of that distribution. For clarity, we have only depicted the quartiles for nonconsecutive mass intervals. We only show the median and quartiles for redshift bins where we detect more than 10 galaxies within a given stellar mass interval. Dashed lines mark the redshift ranges where our sample is less than 75% complete for the given mass interval. [*See the electronic edition of the Journal for a color version of this figure.*]

There is a continuous increase of the specific SFR of the universe as we move to higher redshifts. If we consider the evolution of the specific SFR for different stellar mass intervals (colored lines in Fig. 8), we clearly see that the most massive galaxies ($M > 10^{11.7} M_\odot$) presented very large specific SFRs at high redshift. These galaxies exhibit values of the SFR that are so large that they could double their stellar mass in just 0.1 Gyr (see the scale on the left axis) at $z = 3$–4.[7] As we move to lower redshifts, their specific SFRs decrease considerably, by a factor of 10 from $z \sim 4$ to $z \sim 2.5$ (in less than 1.5 Gyr), and by a factor of ~ 100 from $z \sim 4$ to $z \sim 1.5$ (in 3 Gyr), in agreement with the results from Papovich et al. (2006). For lower stellar masses, the evolution is less pronounced. For example, galaxies with $10^{10.0} < M < 10^{11.0} M_\odot$, whose evolution is very similar to the cosmic average, present a decrease in the specific SFR of a factor of 10 from $z \sim 2.5$ to $z \sim 0.5$ (in 6 Gyr). The evolution at $z < 1$ is very similar for all the stellar mass intervals, as already noted by Zheng et al. (2007), with a change of about a factor of 10 in this period of ~ 8 Gyr. In this period, there is a significant luminosity

---

[7] The individual SFRs and median specific SFRs for the entire sample derived from the extrapolated rest-frame 24 μm luminosities and the calibration given by Alonso-Herrero et al. (2006; see also Calzetti et al. 2007) are a factor of 2–3 smaller at $z \gtrsim 2$ than those derived directly from extrapolated estimations of the total IR luminosity. Papovich et al. (2007) also find (based on 70 μm observations) that SFRs of $z \sim 2$ galaxies obtained from total IR luminosities (extrapolated from fits of dust emission models to single 24 μm detections) are overestimated by factors of a few. Using the SFR estimations based on rest-frame 24 μm luminosities, the median specific SFRs of the most massive galaxies are very similar to the universe average (the shaded area in Fig. 8) at $z = 3$–4, and our global results presented in § 7.2 are not affected.

(and possibly density) evolution of luminous IR galaxies (Chary & Elbaz 2001; Pérez-González et al. 2005). This evolution is also detected in our stellar mass analysis, given that the fraction of the total stellar mass density locked in galaxies emitting strongly in the thermal IR (and being detected by MIPS) increase from about 10% at $z = 0$ to $\sim 50\%$ at $z = 0.7$–1.0, where LIRGs dominate the cosmic SFR density. The fraction of the total stellar mass density locked in MIPS sources remains approximately constant from $z \sim 1$ up to $z = 4$, where LIRGs and even ULIRGs have a significant contribution to the total SFR density, as the comparison with other SFR tracers shows (Pérez-González et al. 2005).

The evolution of the cosmic specific SFR is also consistent with the "downsizing" picture described in § 5.6, where the most massive galaxies formed most of their mass at $z > 3$ in very intense and rapid episodes of star formation, presenting high specific SFRs that would double the stellar mass of these systems in timescales shorter than 1 Gyr. Less massive systems assembled more slowly, presenting specific SFRs which would double their mass in timescales comparable to the look-back time of the universe at each redshift.

8. CONCLUSIONS

We characterize the mass assembly of galaxies in the last 12 Gyr ($\sim 90\%$ of the Hubble time) by analyzing the stellar mass functions and densities estimated from a sample of $\sim 28,000$ sources selected in the rest-frame near-infrared. The sample has been built from *Spitzer*/IRAC (the selection being made at 3.6 and 4.5 μm) observations of three fields: the Hubble Deep Field–North, the Chandra Deep Field–South, and the Lockman Hole. The total surveyed area is 664 arcmin². This IRAC sample is 75% complete down to 1.6 μJy ([3.6]=23.4), which translates to an approximate stellar mass completeness level (for passively evolving galaxies formed at $z = \infty$) of at least $10^9 M_\odot$ up to $z = 0.5$, $10^{10} M_\odot$ up to $z = 1.0$, and $10^{11} M_\odot$ up to $z = 4.0$. In order to analyze the effects on our results of low-mass galaxies that are faint at rest-frame near-infrared wavelengths, we complement the IRAC survey with an optically ($I < 25.5$) selected sample of similar size.

We estimate photometric redshifts, stellar masses, and star formation rates for all galaxies using a set of templates built by modeling the stellar population and dust emission of galaxies with known spectroscopic redshifts. The quality of our photometric redshifts is very good for more than 85% of the sample, and good for nearly 95%, according to the comparison with spectroscopic redshift at $z < 1.5$. At $z > 1.5$, where spectroscopic redshifts are scarce, we test our photometric redshifts by comparing the average values and standard deviations of the redshift distributions of several galaxy populations: Lyman break galaxies (LBGs), distant red galaxies (DRGs), and *BzK* galaxies. We find very good agreement with spectroscopic surveys of these sources, and other photometric redshift analysis. We also analyze the goodness of the stellar mass and star formation rate estimates, finding that they are accurate within a factor of 2–3 (see Appendix B).

Our estimation of the local stellar mass function is in good agreement with previous estimations based on 2MASS data (Cole et al. 2001; Bell et al. 2003). We find a slope of $\alpha \sim -1.2$ at low stellar masses (similar values are also found for stellar mass functions at all redshifts up to $z = 4$), and a pronounced steepening of the stellar mass function at $M < 10^9 M_\odot$. Approximately 1 out of 4 local galaxies are actively forming stars. Around 10%–15% of the global stellar mass density in the local universe is found in active star-forming galaxies (in agreement with Pérez-González

et al. 2003a), and this percentage rises to $\sim 50\%$ at $z \sim 1$, remaining approximately constant beyond that redshift.

Our results indicate that the most massive systems ($M > 10^{12.0} M_\odot$) assembled the bulk of their stellar mass in a very rapid collapse (half of their stellar mass in less than 1 Gyr) at early epochs ($z > 3$, or 11 Gyr ago), close to what can be regarded as a monolithic collapse. The formation was characterized by large specific SFRs with doubling times of about 0.1 Gyr. Galaxies with $10^{11.5} < M < 10^{12.0} M_\odot$ formed more slowly, assembling half of their stellar mass before $z \sim 1.5$ (more than 9 Gyr ago) and more than 90% of their stellar mass beyond $z \sim 0.6$. Less massive systems (with $10^{9.0} < M < 10^{11.0} M_\odot$) formed at even a slower speed: half of their stellar mass was assembled beyond $z \sim 1$ (more than 7 Gyr ago), and they experienced a significant increase in their stellar mass (20%–40%) recently (at $z < 0.4$, or in the last 4 Gyr), probably by dry accretion of small satellite galaxies (with an accretion rate $\Delta M/M = 0.12 \pm 0.03$ Gyr^{-1}). The specific SFRs of these galaxies evolved (closely to the cosmic average) from 10 Gyr^{-1} at $z \sim 4$ to less than 0.1 Gyr^{-1} in the local universe.

We find that approximately half of the local stellar mass density was already formed at $z \sim 1$ (8 Gyr ago), which translates to an average assembling rate of 0.048 $M_\odot$ yr^{-1} Mpc^{-3} (taking into account a 28% recycle factor, i.e., the fraction of the total stellar mass reinjected in the interstellar medium in the form of stellar winds and supernova ejecta). At least another 40% of the local stellar mass density assembled from $z = 1$ to $z = 4$ (in 4 Gyr) at an average rate of 0.074 $M_\odot$ yr^{-1} Mpc^{-3}. We find that the cosmic SFR densities estimated by differentiating the evolution of the cosmic stellar mass density do not match the observations based on direct SFR tracers, as also noticed by Rudnick et al. (2006), Hopkins & Beacom (2006), and Borch et al. (2006). The mismatch up to $z \sim 2$ (a factor of ~ 1.7) could be explained by changing the IMF to a Chabrier (2003) IMF (instead of a Salpeter 1955 IMF, the default used in this paper). At $z \gtrsim 2$, the discrepancy is larger (a factor of 4–5), and can only be solved if the IMF is top-heavy (i.e., a different IMF at high redshift) and/or if the SFRs of the most massive galaxies at $z = 3$–4 (calculated with different star formation tracers, mainly the UV, IR, and submillimeter emission) are overestimated due to, for example, the presence of strong obscured AGNs in most of these sources (which would imply that a significant fraction of their UV or IR emission arises from the AGN, i.e., it is not linked to star formation).

We confirm that galaxy formation follows a "downsizing" scenario (Cowie et al. 1996). Our results are broadly consistent with previous observational works that confirm this formation theory (Heavens et al. 2004; Juneau et al. 2005; Glazebrook et al. 2004; Pérez-González et al. 2005; Fontana et al. 2006), and with models of galaxy formation (e.g., Nagamine et al. 2004; Croton et al. 2006; Bower et al. 2006). At low redshift ($z < 1$), there is also an "upsizing" effect, when intermediate-mass galaxies ($M = 10^9$–$10^{11} M_\odot$) increase their density by accretion or coalescence of previously formed smaller galaxies (producing little star formation).

We have also analyzed the nature of the galaxies in our sample, comparing them with the populations of sources detected with different selection techniques by other surveys. Based on the measured number densities and redshifts, we conclude that our survey constitutes an almost complete census of the different populations of previously known galaxies at high redshifts, including most of the LBGs at $1 < z < 3.5$, most of the DRGs at $z \gtrsim 2$, and most of the BzK galaxies at $z > 1.4$. LBGs dominate the number counts of IRAC galaxies at high redshift, being about a factor of 2–3 more numerous than DRGs and BzK galaxies, but most of the stellar mass density (more than 50% and up to 97%) at $z > 2.5$ resides in the latter, while LBGs account for less than 50% of the total stellar mass density.

APPENDIX A

THE MERGED PHOTOMETRIC CATALOG

This Appendix describes how we selected and measured multiwavelength photometry for the galaxies included in the IRAC and *I*-band selected samples. First, we characterize the reduction, detection, and photometry procedures in the *Spitzer* images. Then, we outline how we merged this photometry with the fluxes estimated in ground-based optical and NIR images. Special details are given for the spectroscopy compiled for our sources. We also discuss the methods used to remove stars from our catalogs. Finally, we discuss the presence of active galactic nuclei (AGNs) in our samples.

A1. IRAC AND MIPS DETECTION AND PHOTOMETRY

We compiled all the IRAC and MIPS data available in the HDF-N, the CDF-S, and the LHF, including the GTO data in the three fields, the GOODS data in HDF-N and CDF-S, and the data around the GOODS footprint in the CDF-S taken as a *Spitzer* Legacy Survey (PI: P. G. van Dokkum). All the reduced data (Basic Calibrated Data products delivered by the *Spitzer Science Center*) were mosaicked together using the procedure developed by Huang et al. (2004). This procedure includes pointing refinement, distortion correction, drizzling to a scale half of the original (approximately 0.6 arcsec pixel^{-1}), and correction of detector artifacts (more noticeably, mux-bleeding).

Detection of sources in the IRAC images was performed with SEXTRACTOR (Bertin & Arnouts 1996). Given that the FWHM of the IRAC point-spread function (PSF) is $1.8''$–$2.0''$ (Fazio et al. 2004a), and that the PSFs are very sharp and stable, almost all sources are pointlike in the four channels, and objects can be resolved for separations of the order of $\sim 1''$. The crowdedness of the our very deep images in the two bluer IRAC bands is very high, mostly at 3.6 μm and especially near bright stars, making the deblending of sources difficult for automatic procedures such as that used by SEXTRACTOR. To alleviate this problem, we detected sources at 3.6 μm and also (separately) at 4.5 μm, where the depth is slightly lower and crowding is less severe. The two catalogs built in the two bluer IRAC bands (at 3.6 μm and 4.5 μm) were merged by removing sources whose separation was smaller than $1''$ (roughly, 1.5 pixels in the mosaicked images). After the selection, we measured aperture photometry in the four IRAC images (fixing the positions and forcing the detection in all bands) following the same technique used by Huang et al. (2004). Fluxes were measured in small apertures of $4''$ diameter with SEXTRACTOR (obtaining almost identical results with other software, such as DAOPHOT, which was used by Huang et al. 2004). The final integrated magnitude was obtained after applying an aperture correction based on empirical IRAC PSFs. The aperture corrections for this $4''$ diameter aperture are 0.32 ± 0.03, 0.36 ± 0.02, 0.53 ± 0.02, and 0.65 ± 0.02 mag for channels 3.6, 4.5, 5.8, and 8.0 μm, respectively, where the uncertainties include the effects of typical World Coordinate System (WCS) random alignment errors (always less than 1 pixel). For sources whose Kron aperture (in optical/NIR bands) was larger than $6''$ (a number chosen by studying our simulations described below), we measured the photometry with a large enough aperture to enclose the entire object and checked the results with the `mag_iso` output given by SEXTRACTOR. We would like to stress that all the sources in the IRAC sample have measured fluxes at both 3.6 and 4.5 μm.

The characterization of the IRAC catalogs (i.e., the analysis of the effects of confusion on the deblending of sources and the photometry) was carried out by simulations consisting of adding artificial sources to the mosaicked images. A given number of sources (7 sources arcmin^{-2}, which is the number of sources corresponding to a Poisson uncertainty in the observed number densities) of a given magnitude were added to the images, and then the full detection and photometry procedure was applied. Bulge-dominated galaxies of different sizes (from $1''$ to $10''$) were also added in the simulation to check the photometry of nearby ($z \lesssim 0.5$) extended objects. By measuring the angular sizes of galaxies in the optical/NIR images, we determined that "extended sources" (defined as sources whose semimajor axis is larger than $6''$; see below) are just a minor fraction of the total number of IRAC sources at $z < 0.5$ (less than 3%), and completely negligible (less than 0.5%) at $z > 0.5$. By checking the fraction of input sources recovered by this procedure (in the same position within $1''$ or 1.5 pixels), we estimated the completeness levels at which our catalogs are reliable (in terms of deblending of sources and photometry) and the accuracy of our photometry. As mentioned in § 2, our IRAC catalogs are 75% complete down to $[3.6] \sim 23.3$ mag.

Our simulations also show that for sources whose semimajor axis is larger than $6''$, aperture photometry in a $4''$ diameter aperture corrected to an integrated flux based on empirical PSFs underestimated (on average) the total flux of these sources (estimated from the `mag_iso` output given by SEXTRACTOR) in more than 10%, i.e., 1–2 times the typical measurement uncertainty (see below). Thus, we considered sources larger than $6''$ as extended sources in IRAC (as also recommended in the *Spitzer*/IRAC cookbook), and for them we estimated integrated fluxes using large apertures enclosing the entire objects and the extended source aperture corrections given in the *Spitzer*/IRAC cookbook.

The errors of the IRAC photometry were estimated from the sky uncertainty (estimated with SEXTRACTOR with a box filtering method), detector readout noise, Poisson noise in the measured fluxes (using the detector gain and total exposure time per pixel), and the uncertainty in the aperture corrections (which include the effect of WCS errors). A 2% absolute calibration uncertainty was also considered (Reach et al. 2005). The final uncertainties were checked with our simulations. For each input magnitude interval, we analyzed the output magnitudes obtained with our photometric procedure. For $[3.6] = 20$ mag, the typical uncertainty is 0.05 mag, and for $[3.6] = 24$ mag, the typical uncertainty is 0.3 mag. For $[4.5] = 20$ mag, the typical uncertainty is 0.05 mag, and for $[4.5] = 24$ mag, the typical uncertainty is 0.4 mag. For $[5.8] = 19$ mag, the typical uncertainty is 0.07 mag, and for $[5.8] = 23$ mag, the typical uncertainty is 0.4 mag. For $[8.0] = 19$ mag, the typical uncertainty is 0.08 mag, and for $[8.0] = 22$ mag, the typical uncertainty is 0.4 mag.

All the MIPS 24 μm data for each field (including GTO and GOODS data) were reduced and mosaicked together using the MIPS Data Analysis Tool (Gordon et al. 2005). We detected sources and measured integrated fluxes using PSF fitting (with the DAOPHOT IRAF[8] package) and aperture corrections. Sources were detected in three passes to recover the faintest sources, many of which are hidden by brighter ones. Photometry was extracted for all the detected sources simultaneously. For sources of noticeable extent (more than $25''$), a large enough aperture was set accordingly. For the rest, a circular aperture of diameter $15''$ (6 pixels) was utilized. For this aperture, a 17% correction in flux must be used to correct to the total flux (based on the theoretical PSF of MIPS). The sky estimation was carried out in two steps, first removing the large-scale variation (due to zodiacal light), and then measuring the background around each source. Based on simulations similar to those carried out with the IRAC data, we estimate that our catalogs are 75% complete at $F(24) = 80$ μJy. Uncertainties based on these simulations are less than 5% for sources with $F(24) > 400$ μJy, and 10% for sources with $F(24) \sim 80$ μJy.

A2. OPTICAL AND NIR PHOTOMETRY

The *Spitzer* data were complemented with other publicly available and proprietary photometric and spectroscopic data in the three fields. For the HDF-N and the CDF-S, the data set is described in detail in Pérez-González et al. (2005). For this paper, we added in the

---

[8] IRAF is distributed by the National Optical Astronomy Observatory, which is operated by the Association of Universities for Research in Astronomy (AURA), Inc., under cooperative agreement with the National Science Foundation.

TABLE 5
Characteristics of the Data Compiled for the Lockman Hole

Band (1)	λ_{eff} (2)	m_{lim} (3)	Source (4)
IRAC-3.6........................	3.561	23.0	*Spitzer* GTO
IRAC-4.5........................	4.510	23.0	*Spitzer* GTO
IRAC-5.8........................	5.689	22.3	*Spitzer* GTO
IRAC-8.0........................	7.958	22.0	*Spitzer* GTO
MIPS-24..........................	23.844	20.0	*Spitzer* GTO
B	0.442	26.0	Subaru Deep imaging[a]
R	0.652	25.4	Subaru Deep imaging[a]
I	0.795	25.0	Subaru Deep imaging[a]
z	0.907	24.5	Subaru Deep imaging[a]
U...................................	0.361	23.1	ING Archive[b]
g....................................	0.486	24.0	ING Archive[b]
i	0.767	22.3	ING Archive[b]
J....................................	1.251	22.5	UKIDSS[c]
H...................................	1.649	20.4	TIFKAM[d]
K...................................	2.208	22.9	UKIDSS[c]

Notes.—Col. (1): Name of the observing band. Col. (2): Effective wavelength (in μm) of the filter+detector. Col. (3): Limiting AB magnitudes defined as the third quartile of the magnitude distribution of our sample. Col. (4): Source from which the data were obtained.

[a] Publicly available ultradeep optical data from the SMOKA Subaru Archive, taken with the Suprime-Cam instrument on the Subaru Telescope.

[b] Data obtained from the Archive of the Isaac Newton Group of Telescopes, and taken with the Wide Field Camera on the 2.5 m Isaac Newton Telescope.

[c] Data provided by the UKIRT Infrared Deep Sky Survey (UKIDSS), data release 2 (DR2, Lawrence et al. 2007).

[d] Data taken with the TIFKAM instrument on the 2.1 m telescope at Kitt Peak National Observatory.

HDF-N the *JK* data described in V. Villar et al. (2008, in preparation; with limiting magnitudes[9] $J = 22.4$ and $K = 21.4$), *GALEX* data extracted from the *GALEX* archive (with limiting magnitudes NUV $= 24.9$ and FUV $= 25.3$), the spectroscopic redshifts published by Reddy et al. (2006a), and the GOODS IRAC and MIPS data. In the CDF-S, we added an image of size $37' \times 30'$ taken in the NB816 filter with the Suprime-Cam instrument on Subaru (with a limiting magnitude of NB816 $= 24.8$), the spectroscopic redshifts published by Vanzella et al. (2006), and the GOODS and *Spitzer* Legacy Survey (PI: P. G. van Dokkum) IRAC and MIPS data. For the LHF field (not used in Pérez-González et al. 2005), we summarize the main characteristics of the data set, including the wavelengths, limiting magnitudes, and references for each filter in Table 5. The Subaru observations in the CDF-S and the LHF were obtained from the SMOKA Subaru Archive, and reduced using their pipeline SDFRED v1.2. The photometric and astrometric calibration was carried out by comparison with the Sloan Digital Sky Survey (SDSS DR4; Adelman-McCarthy et al. 2006) catalogs. The ING data were provided (fully reduced and calibrated) from the CASU INT Wide Field Camera Survey (Barcons et al. 2002; Yuan et al. 2003). The *H*-band TIFKAM data (Le Floc'h et al. 2004) were reduced following typical NIR procedures, and the photometric and astrometric calibration obtained through comparison with Two Micron All Sky Survey (2MASS) catalogs. The UKIDSS data were provided (fully reduced and calibrated) by the UKIRT Infrared Deep Sky Survey (UKIDSS DR2; Lawrence et al. 2007). All the images in our complete data set were calibrated photometrically (using direct observations of SDSS and 2MASS catalogs) and astrometrically (using SDSS and 2MASS catalogs). Typical absolute photometric uncertainties were 0.03 mag, and the WCS absolute uncertainty was always less than $0.5''$.

A3. MERGED PHOTOMETRIC CATALOG

Aperture-matched photometry in all bands was carried out using the procedure described in Pérez-González et al. (2005). The coordinates of the IRAC detected sources are cross-correlated with each of the UV, optical, and NIR catalogs using a search radius of $2.5''$ (roughly 2 pixels in the original IRAC images) and starting by the deepest images. Once the source was identified in one of these image (for most cases, the first one), we took the Kron (1980) elliptical aperture best enclosing the entire source from this reference image, and translated it to all the other bands. The aperture was large enough to enclose the PSF (at least twice the FWHM of the PSF) in all UV/optical/NIR images (the seeing was always less than $1.5''$). By randomly varying the center of this aperture in each image, we checked that small WCS errors did not affect the integrated apertures significantly (the variations were always well within the photometric uncertainties). For IRAC and MIPS, where the PSFs are comparatively large, we assumed the integrated magnitude measured in small apertures (applying aperture corrections), as discussed previously. For *GALEX* data, given that the FWHM of the PSF is $6''$–$7''$ (depending on the band, position in the detector, and brightness of the source), we took the mag_best magnitude given by SEXTRACTOR. For *Hubble Space Telescope* (*HST*) images, we picked the integrated flux of the closest source measured with SEXTRACTOR, not carrying out any aperture matching. For this reason, *HST* fluxes were not used in the photometric redshift and stellar mass determination.

---

[9] Defined as the third quartile of the magnitude distribution of our sample.

Uncertainties of each measured flux were obtained from the sky pixel-to-pixel variations, detector readout noise, Poisson noise in the measured fluxes (taking into account the detector gain and total exposure time per pixel, which were combined to give rms images of the fields), the errors introduced by the uncertainties in the WCS, and the uncertainty in the absolute photometric calibration (typically 0.03 mag). Reductions involving drizzling (e.g., in ACS or IRAC images), non-integer pixel shifts (e.g., NIR images), and also detector artifacts or unresolved faint sources, mean that uncertainties derived uniquely from pixel-to-pixel variations of adjacent sky pixels underestimate the real noise, since these effects correlate the signal of nearby pixels (see, e.g., Casertano et al. 2000; Labbé et al. 2003; Gawiser et al. 2006; Quadri et al. 2007). To account for this, we estimated the background level and noise in three different ways. First, we measured the average signal per pixel and noise in a circular corona $5''$ wide surrounding the Kron photometric aperture for each source, scaling the noise with a $N^{1/2}$ factor, where N is the number of pixels of the source photometric aperture. To get rid of the effect of correlated noise in this estimation of the uncertainty introduced by the pixel-to-pixel variance, we also estimated the background level and noise using 20 artificial apertures of the same size as used for the source. These artificial apertures were built by randomly selecting (in general, non-adjacent) "sky pixels" in a $1' \times 1'$ box around the source. Those "sky pixels" excluded pixels whose signal was $5\,\sigma$ above the rms value estimated with the first method. The average signal and standard deviation of the integrated fluxes within these artificial apertures provided another (less biased) estimation of the background level and noise. Finally, we also used 20 apertures of the same size, shape, and orientation as the source photometric aperture in the $1' \times 1'$ box, meaning that more than 90% of their pixels were "sky pixels" (as defined above), and applying the method described in Labbé et al. (2003). The final background level was set to the average of the three estimations, and the background noise was set to the largest estimation provided by any of the three previously described methods. In practice, the largest estimation of the noise was, in most cases, provided by the second method: on average, the noise was 10%–20% higher than what was obtained with the first method (which proves the importance of correlated noise), and less than 5% higher than the third method.

The validity of the method used to obtain merged photometry from the UV to the MIR bands was tested by comparing the measured colors with those obtained from images convolved to the same resolution. For this test, we matched the PSFs of an optical image (the I-band) to that of the IRAC 3.6 μm channel (which is worse) using the IRAF `psf` task (which produces a convolution kernel to match the optical PSF to the IRAC PSF). We then measured photometry in a $4''$ diameter aperture in both bands and obtain $I - [3.6]$ colors for all the detected sources. Note that since both images have the same PSF, any aperture size could in principle be used to obtain colors, but very small apertures would be more affected by WCS and PSF matching errors. In the case of resolved nearby sources, very small apertures could also bias the results if the colors are not uniform across the galaxy. The colors derived with this method were very similar to those obtained with our photometric procedure. The absolute mean difference between the two methods was $\langle |\Delta(I - [3.6])| \rangle = 0.02$ mag (the average difference was $\langle \Delta(I - [3.6]) \rangle = 0.005$ mag), and the scatter 0.11 mag, comparable to the color uncertainties (the average is 0.15 mag). The average difference is independent of the integrated magnitude and size. For sources with $I < 22$, we find $\langle \Delta(I - [3.6]) \rangle = 0.004 \pm 0.12$ mag, for sources with $22 < I < 24$ we measure $\langle \Delta(I - [3.6]) \rangle = 0.01 \pm 0.11$ mag, and for sources with $I > 24$ we obtain $\langle \Delta(I - [3.6]) \rangle = -0.02 \pm 0.12$ mag. For sources smaller than $6''$, we find $\langle \Delta(I - [3.6]) \rangle = -0.01 \pm 0.12$ mag, and for larger galaxies we find $\langle \Delta(I - [3.6]) \rangle = 0.006 \pm 0.11$ mag.

For some of the IRAC sources (10%–15% of the entire IRAC sample in each field), there were several UV/optical/NIR counterparts in ground-based images for one single IRAC source within the $2.5''$ search radius. For these sources, we remeasured the IRAC fluxes by fixing the positions of the blended objects and deconvolving the images using the IRAC PSFs. Although the IRAC PSFs have FWHMs of approximately $2''$, the central position of each IRAC source can be determined more accurately (the actual value depending on the brightness of the source), and sources are resolved for separations of the order of $\sim 1''$. This means that if the source positions are known, we can identify and deblend IRAC sources separated $\sim 1''$ from each other. We adopted a deconvolution method similar to that used in Grazian et al. (2006). The ground-based optical/NIR reference image was used to measure the positions of the different blended sources. Then, the reference image and the IRAC images were realigned locally (in a $1' \times 1'$ square region around the source) to minimize the WCS related errors in the photometry, which were expected to be large in the very small apertures used in the deconvolution method. The IRAC photometry in this case was measured by convolving the IRAC PSF with the reference image PSF and scaling the flux of each object to match the IRAC fluxes in an aperture of $0.9''$ (~ 1.5 pixels in the IRAC images). For this aperture size, the aperture correction of the IRAC bands are 1.01 ± 0.07, 1.02 ± 0.08, 1.2 ± 0.10, and 1.44 ± 0.14 mag for channels 3.6, 4.5, 5.8, and 8.0 μm, respectively (including WCS errors). For the separations between the sources that we are trying to deconvolve (separations larger than $1''$ and smaller than $2.5''$), the flux contamination from the surrounding sources to a given one was, in most cases, lower than a 10% of the flux in the photometric aperture. The artificial source simulations validated this procedure.

Most of the IRAC selected sources are detected in our deepest Subaru images in the HDF-N: approximately 90% are detected in B, R, and/or I. In these bands, 75% of our sources are brighter than $B = 25.5$, $R = 24.9$, and $I = 24.5$. In the CDF-S, 90% of the sources are detected in the NB816 filter, and 75% of them are brighter than NB816 $= 24.8$. In the same field, about 70% of sources are detected in B (75% of them are brighter than $B = 25.3$), 60% in R (75% of them brighter than $R = 24.8$), and 40% in I (75% of sources brighter than $I = 23.7$). MIPS at 24 μm is able to detect about 25% of the IRAC sources (75% of them above $F(24) = 40$ μJy).

More than 90% of the I-band selected sources (see § 2) were also detected in deep $BVRz$ imaging. In these bands, 75% of our I-band sources are brighter than $B = 26.0$, $V = 25.8$, $R = 25.5$, and $z = 25.1$. About 50%–55% of the I-band sample is detected by IRAC (at 3.6 and 4.5 μm; at 5.8 and 8.0 μm, the fraction drops to 40%–45%). MIPS at 24 μm is able to detect about 7% of the I-band sources above $F(24) = 80$ μJy.

A negligible fraction of the entire IRAC sample (less than 3%, not large enough to change our results significantly) was detected in less than 5 filters (our limit to calculate a reliable photometric redshift), all of these galaxies presenting fluxes below the 75% completeness level. For the I-band selected sample, only 2% of the sources are detected in less than 5 filters.

A4. THE SPECTROSCOPIC SAMPLE

Both the HDF-N and the CDF-S include a large compilation of spectroscopic redshifts obtained by several surveys. Unfortunately, there is no public spectroscopic survey in the LHF, so this field could not be used for building templates to estimate photometric redshifts

(see § B.4). In the HDF-N, we used 1699 spectroscopic redshifts (∼20% of the entire sample in that field) found in Wirth et al. (2004), Cowie et al. (2004), and Reddy et al. (2006a). Only a fraction of those redshifts (1340 sources) are flagged as high reliability (larger than 80%). In the CDF-S, we compiled 1410 spectroscopic redshifts (about 15% of the sample in that field), 891 of them flagged as reliable with a probability larger than 80%, from several sources: Le Fèvre et al. (2004), Szokoly et al. (2004), Vanzella et al. (2005), and Vanzella et al. (2006). More than half of the highly reliable spectroscopic redshifts are below $z = 1.0$ (55% in the CDF-S, and 80% in the HDF-N), and most of them are below $z = 1.5$ (95% in the CDF-S, and 97% in the HDF-N). These spectroscopic redshifts were complemented with photometric redshifts estimated, as explained in § B.4.

A5. STAR-GALAXY SEPARATION

In order to separate galaxies from stars in the merged photometric catalogs, we used eight criteria, one based on the STELLARITY parameter given by SEXTRACTOR (Bertin & Arnouts 1996), and the other seven criteria based on color-color and color-magnitude diagrams using optical and NIR fluxes. All objects detected in more than one optical or NIR band, and presenting an average value of the STELLARITY parameter larger than 0.95, were identified as stars. An object was also considered a star if it satisfied any of these color equations (when fluxes were available), extracted from Eisenhardt et al. (2004) Rowan-Robinson et al. (2005), and Daddi et al. (2004): (1) $[3.6] - [8.0] > -2$, $[3.6] - [8.0] < -1$, and $[8.0] < 20.$, or $[3.6] - [4.5] > -1$, $[3.6] - [4.5] < -0.5$, and $[4.5] < 19.5$; (2) $[5.8] - [8.0] > -1$, $[5.8] - [4.5] < -0.2$, and $[8.0] < 20.$; (3) $I - [8.0] < -1$, or $I - [3.6] < 1$ and $[3.6] < 18.$, or $I - [8.0] < -1$ and $[3.6] - [8.0] < -1$; (4) $B - I > 2 \times (I - [3.6]) + 0.070$; (5) $J - K + 0.956 < 0.5$; (6) $[3.6]_{3''} - 0.460 - [3.6]_{auto} > -0.25$, $[3.6] < 15$, and $[3.6]_{3''} - 0.460 - [3.6]_{auto} < 0.2$, or $[3.6]_{3''} - [3.6]_{auto} < -0.25$, where $[band]_{3''}$ is the magnitude in a $3''$ diameter aperture, and $[band]_{auto}$ is the mag_auto magnitude given by SEXTRACTOR (an estimation of the integrated magnitude); and (7) $z - K < -0.5 + 0.29(B - z)$. The star−galaxy separation for the IRAC sample was checked against the galactic number counts published by Fazio et al. 2004a (see also the stellar number counts predicted by Arendt et al. 1998 and Wainscoat et al. 1992), finding very good agreement with our results (absolute differences of less than 0.1 dex at all fluxes down to the limits of our survey). Note that these authors also show that the stars dominate the number counts at the bright end, but they are a minor contributor at faint magnitudes (less than 4% of the sources at $[3.6] > 20$ are stars), the range where our extragalactic analysis is concentrated. We have also checked that our star detection is able to recover more than 95% of the stars in our IRAC sample that have been spectroscopically confirmed: we identify 222 stars out of 232 spectroscopically confirmed stars in the HDF-N, and 78 out of 82 sources in the CDF-S. All the objects considered stars by the spectroscopy and missed by our algorithm are extended (had effective radii larger than 3 pixels and FWHM larger than 4 pixels) in the ACS images. In the HDF-N, our star detection algorithm identifies six spectroscopically confirmed galaxies as stars, all of them being point-like in the ACS images. In the CDF-S, 14 sources with a spectroscopic redshift are identified as stars by our algorithm, all but two of which are pointlike in the ACS images.

A6. AGN IDENTIFICATION

We used X-ray data (covering our entire surveyed regions in the 3 fields) to select candidates to harbor an AGN within our sample. In the HDF-N, we used the catalog for the 2 Ms Chandra Deep Field-North Survey published by Alexander et al. (2003), finding an X-ray counterpart[10] for 5% of our IRAC sample in that field (3% of the *I*-band sample). In the CDF-S, we used the catalogs published by Giacconi et al. (2002; see also Tozzi et al. 2006) for the 1 Ms Chandra Deep Field-South Survey, identifying 3% of our IRAC sources as X-ray emitters (2% of the *I*-band sample). In the LHF, we identified AGN candidates using the *XMM-Newton* catalogs published by Hasinger et al. (2001; see also Lehmann et al. 2000 and Mainieri et al. 2002a), finding an X-ray counterpart for 0.4% of the IRAC sources in that field (0.2% of the *I*-band sample). In the total IRAC sample, 3% of galaxies at any redshift were identified as X-ray emitters (2% of the entire *I*-band sample), with slightly larger values (4%–6% of all IRAC sources) found for sources at $z > 1.5$. Observations in X-rays are known to miss very obscured AGNs (e.g., Rigby et al. 2004; Donley et al. 2005). Other selection procedures have been used to identify obscured AGNs, such as the presence of a power-law spectrum in the IRAC bands (Alonso-Herrero et al. 2004; Donley et al. 2007). These power-law galaxies (some also detected in X-ray or radio data) are also a very small fraction of our IRAC selected sample, less than 1% of the total number of sources. We refer the reader to § B.6 for a discussion of the characterization of the X-ray sources and the effect of AGN contamination in our results.

APPENDIX B

ESTIMATION OF PHOTOMETRIC REDSHIFTS, STELLAR MASSES, AND STAR FORMATION RATES

B1. STELLAR POPULATION SYNTHESIS MODELS

For the stellar population synthesis models of the SEDs of the spectroscopic sample, we carried out two sets of fits: (1) one set assuming that the star formation history of each galaxy can be described by a declining exponential law with timescale τ, age t [i.e., SFR$(t) \propto e^{-t/\tau}$], metallicity Z, and attenuated by an amount described by the quantity $A(V)$ (hereafter 1-POP models; see also Gil de Paz & Madore 2002); and (2) another set (2-POP models) assuming one recent instantaneous burst of star formation of age t_{you}, metallicity Z_{you}, and extinction $A(V)_{you}$, superimposed on an evolved stellar population characterized by τ_{old}, t_{old}, Z_{old}, and $A(V)_{old}$. The attenuation at any wavelength was calculated from the free parameter $A(V)$ using the Charlot & Fall (2000; hereafter CF00) recipe. In this work, the attenuation of the gas and stellar emissions is divided into three components, based on a simple scenario: the light arising from the newly

---

[10] Our galaxies were cross-correlated with the X-ray catalogs using a $2''$ search radius, as done by Rigby et al. (2004) to match sources at large off-axis angles in the *Chandra* images.

formed stars, embedded in a birth cloud, is attenuated by the material in the H II region, by a surrounding shell of molecular and/or non-ionized atomic gas and dust, and finally by the interstellar medium. The extinction law is approximated by a power-law function of the form $A_\lambda \propto \lambda^n$ (the authors suggest $n = -0.7$). There is also a dependence of the birth cloud extinction on the age of the stars: for stars younger than 10 Myr (the typical lifetime of molecular clouds) the extinction is μ times larger than for older stars, where $\mu \sim 0.3$ (with significant scatter). We also ran a set of models assuming that the attenuation law was similar to the one found for local starbursts by Calzetti et al. (2000, hereafter CALZ00) recipe. The stellar emission in our models was taken from the PEGASE code (Fioc & Rocca-Volmerange 1997), assuming a Salpeter (1955) initial mass function (IMF) with $0.1 < M < 100\,M_\odot$ and a single power-law slope through the entire mass range. We also added the emission from the hydrogen gas heated by the stars (emission lines and nebular continuum) using the emission and recombination coefficients given by Ferland (1980) for an electron temperature $T_e = 10^4$ K, the relations given by Brocklehurst (1971) and the theoretical line ratios expected for a low-density gas ($n_e = 10^2$ cm^{-3}) with $T_e = 10^4$ K in the recombination case B (Osterbrock 1989).

The 1-POP models required four parameters to fit. Our fitting routine probed the solution space in the following ranges for the parameters $[\tau, t, Z, A(V)]$: (1) we assumed τ values from an almost instantaneous burst ($\tau = 1$ Myr) to an almost constant SFR ($\tau = 100$ Gyr) using a logarithmic interval of 0.1 dex (in yr) for a total of 51 steps; (2) ages were probed from $t = 1$ Myr to $t = 13.5$ Gyr in logarithmic intervals for a total of 60 steps, constraining the solution for each object so the computed age was not larger than the age of the universe at the redshift of the galaxy; (3) we used the seven discrete values of the metallicity available in the PEGASE code, 0.005, 0.0.02, 0.2, 0.4, 1.0, 2.5, and 5.0 $Z_\odot$; and (4) extinction values ranged from $A(V) = 0$ mag to $A(V) = 5$ mag in intervals of 0.10 mag (51 steps).

For the 2-POP models, each of the two stellar populations requires in principle four parameters to fit, but we forced the recent burst to be instantaneous, so the young stellar population only requires three free parameters to fit. Added to those seven parameters, one more parameter is necessary, the burst strength b, to describe the fraction of the total stellar mass of the galaxy that the recent burst has created. Our fitting routine probed the solution space in the following ranges for the parameters $\tau_{old}, t_{old}, Z_{old}, A(V)_{old}, \tau_{you}, t_{you}, Z_{you}, A(V)_{you}$, and b: (1) $\tau_{old} = 1$ Myr to $\tau_{old} = 100$ Gyr using a logarithmic interval of 0.1 dex; (2) $t_{old} = 1$ Gyr to $t_{old} = 13.5$ Gyr in logarithmic intervals (constrained by the age of the universe at the redshift of each galaxy); (3) $Z_{old} = 0.005, 0.0.02, 0.2, 0.4, 1.0, 2.5$, and 5.0 $Z_\odot$; (4) $A(V)_{old} = 0$ mag to $A(V)_{old} = 5$ mag in intervals of 0.1 mag; (5) we assumed an instantaneous burst for the recent star formation event (i.e., $\tau_{you} = 1$ Myr, so actually this is not a free parameter); (6) $t_{you} = 1$ Myr to $t_{you} = 1$ Gyr in logarithmic intervals (constrained by the age of the universe at the redshift of each galaxy); (7) $Z_{you} = 0.005, 0.0.02, 0.2, 0.4, 1.0, 2.5$, and 5.0 $Z_\odot$; (8) $A(V)_{old} = 0$ mag to $A(V)_{old} = 8$ mag in intervals of 0.1 mag; and (9) the burst strength could take values from 0.5% to 15% in steps of 0.5%.

B2. STELLAR POPULATION SYNTHESIS FITTING PROCEDURE

The stellar population synthesis models were compared with the observed photometric data of the galaxies in the spectroscopic sample using a maximum likelihood estimator similar to the one defined in equation (6) of Pérez-González et al. (2003b), which takes into account the uncertainties in each data point. All data points for rest-frame wavelengths bluer than 4 μm (where stars should dominate the integrated emission of the galaxy in most cases) were included in the fit.

Given the large number of possible solutions (1×10^6 in the 1-POP case and 3×10^{11} for the 2-POP models), the amount of photometric data to fit (up to 48 bands in the case of the sources in the CDF-S, 16 in the HDF-N, and 14 in the LHF), and the number of galaxies in our samples (more than 50,000 adding IRAC and *I*-band selected galaxies), the time requirements to probe the complete solution space for each galaxy (each one at a certain redshift) were prohibitively high. Therefore, we had to use a minimization procedure to search for the best solution without evaluating the minimization function at all points in the grid of solutions. The minimization procedure was a two-step algorithm. First, we used a genetic algorithm (Charbonneau 1995). This procedure started with 200 "individuals" (i.e., 200 points in the solution space), whose "genome" was formed by the 4 or 8 free parameters in our minimization problem. The 200 individuals were "coupled" randomly (obtaining 100 couples). Each one of these couples (formed by "parents") produced 2 "descendants." Each descendant was built by randomly combining the parameters of the parents. The "genome" of the descendant had to be a better solution for the minimization problem than the "genome" of its parents. If, after building 10 descendants for a given couple, none or only one of them were better solutions to the minimization problem, the two best individuals (the best solutions to the minimization problem) were kept for the next generation, and the rest discarded. After every 10 combinations of parameters, we allowed a random mutation in one of them. After all the couples had produced 2 descendants, we eliminated the parents or descendants that produced the worst results for the minimization problem until 200 individuals survived, and then started again the procedure for another generation with the best 200 individuals. The total number of generations was set to 100. For the final generation, we took the 4 best individuals (the best 4 solutions of the minimization problem) and produced small grids of solutions around them (with a width equal to one-tenth of the full size of the solution space for each free parameter). We evaluated all the solutions in these grids, and found the best solution and confidence intervals. Our minimization procedure was tested for a subsample of 1000 galaxies in the 1-POP case by comparing the best solution found by the algorithm with that obtained by evaluating all the grid points in the entire solution space. For this test sample, the minimization algorithm recovered the best solution for $\sim$50% of the galaxies. For the rest of sources, the difference between the best value and the value recovered by the minimization algorithm was always smaller than or equal to one-tenth of the size of the grid for each free parameter. We will come back to the discussion of the goodness of the minimization algorithm in § B.5, when we discuss the quality of the derived photometric redshifts, stellar masses, and SFRs.

B3. DUST EMISSION MODELS

Once the stellar spectrum was modeled, we subtracted the predicted fluxes from the photometric data points at rest-frame wavelengths redder than 4 μm (if present) to obtain the emission arising from the dust. This "IR excess" was then fitted with one of the dust emission models of Chary & Elbaz (2001). We selected the model best reproducing the colors of the dust emission, if several photometric points were available (for relatively low redshift; see the second SED fitting example in Fig. 9), or the model giving the closest value to the
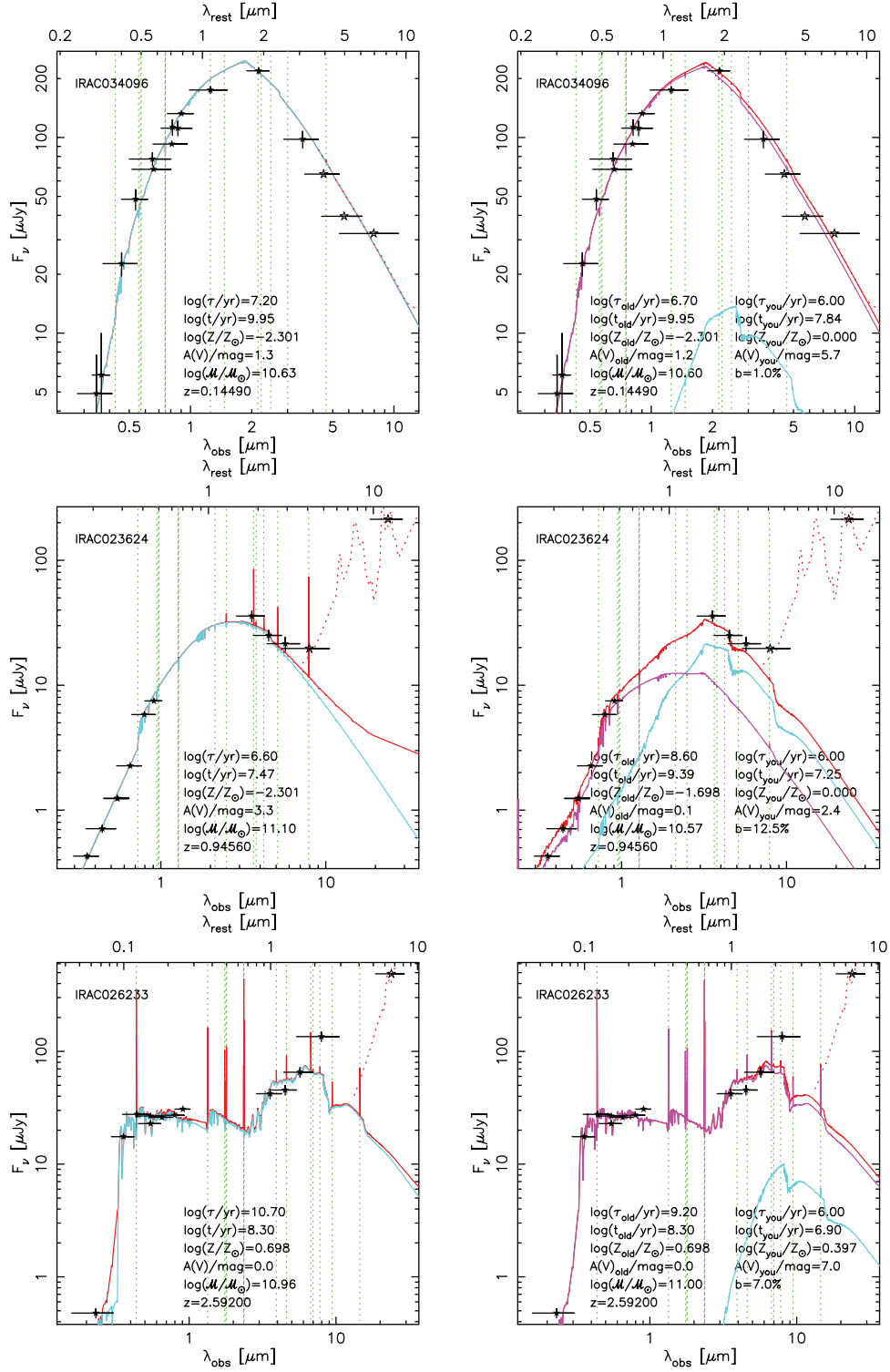
FIG. 9.—Three examples of the stellar population and dust emission modeling of IRAC selected sources in the spectroscopic sample. The spectroscopic redshift and main stellar population parameters of the best fit are given in each panel. Filled black stars and vertical error bars show the photometric points used in the stellar population fits (wavelengths bluer than 4 μm). Horizontal error bars for each photometric point show the width of the filter. Open black stars are the photometric data points used in the modeling of the dust emission. The left panel of each row shows the 1-POP stellar emission fits with a cyan line, and the final fit (including nebular continuum and emission lines) with a solid red line. On the right panel of each row, the same SEDs have been fitted with the 2-POP models, where one stellar population is plotted with a cyan line, the other population with a magenta line, and the addition of both with a red line (including nebular continuum and emission lines). For all panels, the dust emission model taken from Chary & Elbaz (2001), which best reproduces the MIR emission (if present), has been plotted with a dashed red line. Green vertical lines show the positions of the most interesting emission lines in the optical and NIR spectral ranges.

observed monochromatic luminosity if only one IR photometric point was available (see the third example in Fig. 9). To check the uncertainties in the derived IR-based SFRs, we also used the models of Dale & Helou (2002) and G. H. Rieke et al. (2008, in preparation) in the fitting of the "IR excess." The latter are empirical spectral templates constructed largely as described in Donley et al. (2007) Appendix A. For ULIRGs, we used spectra from Armus et al. (2007) for the star-forming galaxies IRAS 1211, 1434, 1525, 2249, in addition to the data on Arp 220 and IRAS 17208 described by Donley et al. (2007). For LIRGs, we used IRS spectra from a MIPS GTO program led by A. Alonso-Herrero. Where the LIRGs were expected to be extended at the scale of the IRS slit width, they were mapped. The mapping data were reduced using CUBISM, written by J. D. Smith as part of the SINGS legacy program.[11] The mapped spectra were collapsed into a single one to represent the integrated galaxy properties. For all the spectra, the templates were extended to shorter wavelengths as described in Donley et al. (2007); by constraining spectral segments with large beam photometry from 2MASS and IRAC, we are able to assemble reliable templates. Toward long wavelengths, we collected photometry from *IRAS*, *ISO*, *Spitzer*, and submillimeter facilities from NED. These data were fitted with a single blackbody with wavelength-dependent emissivity as λ^{β}.

B4. PHOTOMETRIC REDSHIFTS, STELLAR MASSES, AND SFRs

Our final reference template set is composed of 2074 galaxies (1310 galaxies from the HDF-N and 764 from the CDF-S), for which we obtained 1666 different 1-POP+dust models (each with a unique combination of the free parameters), and 1958 2-POP+dust models. As mentioned above, these galaxies were selected from the spectroscopic sample, all of them having a spectroscopic redshift measured with a reliability probability larger than 80%. In addition, all the reference sources should have more than 10 different photometric data points in their SEDs, covering the UV, optical, and NIR/MIR spectral ranges. Three examples of these templates are shown in Figure 9, and discussed in § B.5. The entire template set is available on request to the authors.

The photometric redshift estimation for each galaxy in our survey was carried out with our own code in a way similar to that described in Pérez-González et al. (2005). Briefly, the observed data (fluxes and uncertainties) were compared with the redshifted models (with steps of $\Delta z = 0.01$) using a χ^2 minimization algorithm (such as the one used by Bolzonella et al. 2000). The method compared the photometry with the convolutions of the different filters with the redshifted templates, and determined the best template (the one giving the lowest χ^2 value) for each redshift. The technique also included a preliminary independent detection of the 1.6 μm bump feature (if present), which helped to constrain the final solution and get rid of outliers. The template giving the best solution at each redshift also had to provide an age of the stellar population younger than the age of the universe at that redshift. The photometric redshift probability distribution was built with the best values of the χ^2 estimator (corresponding to the model best reproducing the observed SED) at each redshift, and the most probable redshift and uncertainty were estimated from that probability distribution (as a mean weighted with the probabilities; see Bolzonella et al. 2000).

From the best model and most probable photometric redshift, we can also simultaneously obtain an estimation of the stellar mass, as the model established the monochromatic luminosity per unit of stellar mass at all wavelengths. By scaling this model to the observed monochromatic luminosities (multiplying by a factor), we obtained the stellar mass of each galaxy. The final stellar mass and associated uncertainty for each galaxy were obtained as the average and standard deviation of the stellar masses obtained for each observed photometric band. The uncertainty includes both the effect of the photometric errors and the uncertainty in the determination of the redshift. These errors are estimated for each galaxy by considering the photometric redshift uncertainty and outliers derived from Figure 10 for a galaxy in the same redshift and magnitude intervals, and studying how variations in the redshift affect the mass-to-light ratios in each band and the final stellar mass estimate. The average stellar mass uncertainty is 0.2 dex, typical of any stellar population study (the typical accuracy of stellar masses obtained with stellar population synthesis models is a factor of 2–3; see, e.g., Pérez-González et al. 2003c; Kauffmann et al. 2003; Papovich et al. 2006; Fontana et al. 2006).

Star formation rates were estimated from the total IR luminosity [$L(8$–$1000)$] calculated by integrating the dust emission models for each galaxy between 8 and 1000 μm. Galaxies not detected by MIPS at 24 μm were assumed to have an upper limit flux of $F(24) = 60$ μJy. The final SFR estimation also includes the contribution from unobscured star formation detected directly in the UV. According to Bell et al. (2005), we can estimate the total SFR for each galaxy from $L(8$–$1000)$ and $L(0.28)$, where $L(0.28) = \nu L_{\nu}(0.28)$ is the monochromatic luminosity at 0.28 μm measured directly from the stellar population model for each galaxy. The conversion factor is taken from Kennicutt (1998) for a Salpeter (1955) IMF:

$$\mathrm{SFR} = 1.8 \times 10^{-10}[L(8\text{–}1000) + 3.3L(0.28)]/L_{\odot} \ M_{\odot} \ \mathrm{yr}^{-1}. \tag{B1}$$

In order to characterize the uncertainties of the SFRs derived with our models, we also calculated IR-based SFRs by estimating monochromatic luminosities at rest-frame wavelengths 6.7 μm, 12 μm, and 15 μm. The integrated luminosity $L(8$–$1000)$ can be obtained from these monochromatic luminosities by applying the empirical relationships found in Chary & Elbaz (2001). Another estimation of the SFR can be obtained from the rest-frame monochromatic luminosity at 24 μm, applying the equation given in Alonso-Herrero et al. (2006). We discuss the uncertainties in the SFR estimations in § B.5.4.

B5. EVALUATION OF THE MODELING PROCEDURE AND DERIVED PARAMETERS
B5.1. *Some Examples of SED Fits*

Figure 9 shows three examples of the dust and stellar population models for IRAC sources at different redshifts. The three panels on the left show the fits for the 1-POP case, and the three panels on the right show the fits for the 2-POP case for the same sources.

---

[11] A description of the CUBISM software can be found at http://ssc.spitzer.caltech.edu/archanaly/contributed/cubism/.
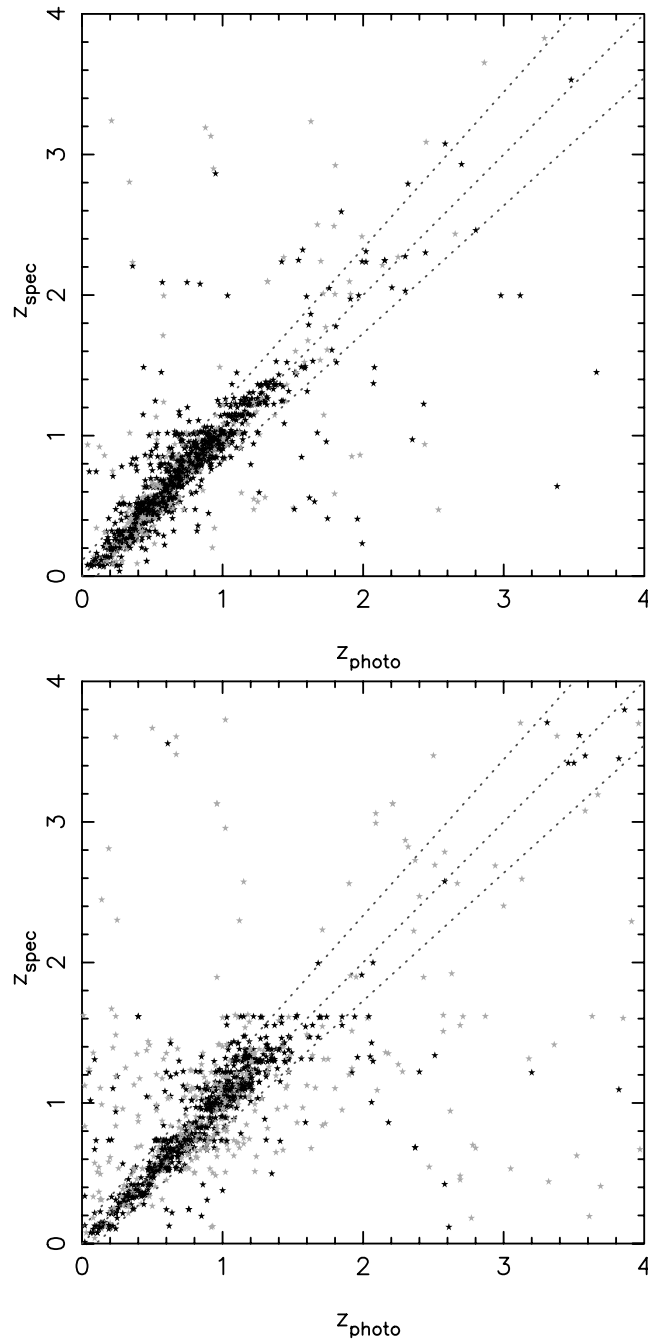
Fig. 10.—Comparison of the spectroscopic and photometric redshifts for IRAC selected sources in the HDF-N (*top panel*) and the CDF-S (*bottom panel*). Gray symbols are sources with spectroscopic redshifts which have a reliability probability lower than 80%. Open stars are sources detected in less than five bands. The dashed lines show the equality line, and the $\sigma_z/(1+z) < 0.1$ area. [*See the electronic edition of the Journal for a color version of this figure.*]

The upper two panels present a source nicely fitted by a single old stellar population with intermediate extinction, no current star formation (a bulge-dominated galaxy), and no detection at 24 μm. In this case, although the photometry at rest-frame wavelengths redder than 4 μm was not used in the model fitting, those points are well reproduced with just stellar emission. When fitting the same SED with a 2-POP model, we recover parameters very similar to the 1-POP case, with a minor contribution (just 1% in mass) from a more recent burst. Note that both types of models give very similar stellar mass values.

The second example (Fig. 9, *middle row*) shows an intermediate-redshift galaxy detected at 24 μm. This galaxy can be fitted either by an old single stellar population with a large extinction or with a combination of an old stellar population with very low attenuation and a more recent burst contributing about 13% to the total stellar mass of the galaxy. This recent burst presents a relatively large dust attenuation that could be responsible for the emission in the MIR/FIR (the galaxy is detected at 24 μm). For this galaxy, dust emits a significant fraction (about 50%) of the 8 μm luminosity (rest-frame 4 μm) and almost 100% of the 24 μm luminosity (rest-frame 12 μm). The 1-POP models give a larger stellar mass value than the 2-POP models (still, the difference is a factor of 3, comparable to the typical uncertainty in stellar population studies) because a lot of stars are necessary to fit the high-NIR photometric data points, while a lot of extinction is necessary to simultaneously fit the UV/optical fluxes.

The third example (Fig. 9, *bottom row*) is a high-redshift galaxy with a very blue spectrum. It can be fitted either with an almost continuous unattenuated star formation (based on the high τ value) lasting about 100 Myr, or with a similar primary burst (producing 93% of all the stellar mass) followed by a more recent (10 Myr) and much more attenuated [$A(V)_{\rm you} = 7$ mag and a strong MIR emission detected at 24 μm] event of star formation. Note also that the IRAC photometric point at 8.0 μm is too high in comparison with the combined star+dust models. At wavelengths around $\lambda \sim 4$–10 μm or even at $\lambda \sim 2$–10 μm for very luminous IR sources (with very hot dust), the integrated emission comes from both the dust and the stars in comparable fractions. In this overlap region between the dust and stellar models, the spectrum may show prominent emission lines, PAH features, or emission from hot dust (e.g., coming from a dust torus surrounding a nuclear massive black hole), which are not found in the stellar and dust emission models. For example, there is a PAH feature at rest-frame 3.3 μm (very weak in all dust models in the Chary & Elbaz 2001 or Dale & Helou 2002 libraries), which may have a nonnegligible contribution to the global emission in this spectral region for very luminous IR sources.

B5.2. *Statistical Evaluation of the Photometric Redshifts*

The main three parameters that we want to extract from the SED fits are the photometric redshift, the stellar mass, and the SFR of each galaxy. The quality of our photometric redshifts is checked in Figure 10 for the fields with extensive spectroscopic data: the HDF-N and the CDF-S. Unfortunately, given that there is not a systematic public spectroscopic survey in the LHF, we cannot check our photometric redshifts directly in this field. In spite of this, the photometry in the LHF is as good or even better (given that the optical images are ultradeep observations taken with Subaru) than in the other two fields, and the general redshift distribution for the LHF sources is similar to that in the HDF-N and the CDF-S. Consequently, we conclude that the quality of the photometric redshifts in the LHF must be comparable to the other two fields (see also the discussion of the redshift distribution of our sample in § 4).

The top panel of Figure 10 shows a comparison of our photometric redshifts and spectroscopic redshifts for the IRAC selected sample in the HDF-N (for the 1702 sources with available spectroscopy). The average (median) redshift difference ($\delta z = z_{\rm spec} - z_{\rm photo}$) is 0.014 (0.010), comparable to the redshift step used in our photometric redshift technique. This demonstrates that there are no systematic errors in our redshifts. Almost all sources, 95%, have values of $\sigma_z/(1+z) < 0.2$ (where σ_z is the absolute value of δz), 88% of the objects present values of $\sigma_z/(1+z) < 0.1$, and 70% have $\sigma_z/(1+z) < 0.05$. The average (median) value of $\sigma_z/(1+z)$ is 0.055 (0.032). Very similar statistics are obtained for the I-band selected sample: 94% of these sources present $\sigma_z/(1+z) < 0.2$, 86% $\sigma_z/(1+z) < 0.1$, and the average (median) $\sigma_z/(1+z)$ is 0.060 (0.036).

The quality of the photometric redshifts in the CDF-S for IRAC selected sources (for the 1410 sources with available spectroscopy) is shown in the bottom panel of Figure 10. The average (median) value δz is 0.020 (0.015). In this field, 93% of the objects have values of $\sigma_z/(1+z) < 0.2$, 85% of the objects have values of $\sigma_z/(1+z) < 0.1$, and 67% have $\sigma_z/(1+z) < 0.05$. The average (median) $\sigma_z/(1+z)$ is 0.060 (0.040). For the I-band selected sources, the numbers are similar: 92% of these sources present $\sigma_z/(1+z) < 0.2$, 80% $\sigma_z/(1+z) < 0.1$, and the average (median) $\sigma_z/(1+z)$ is 0.080 (0.047).

Some of the sources used in the photometric redshift evaluation depicted in Figure 10 were used in the building of the templates (77% of all sources plotted in the HDF-N, and 54% in the CDF-S). The validity of our procedure (including the merging of photometric data) and the templates built with data from the HDF-N and the CDF-S was also tested in completely different and independent fields. For example, in the extended Groth strip (P. G. Pérez-González et al. 2008, in preparation), we compared our photometric redshifts (based on photometry measured in the same way as in this paper) with spectroscopic values for 6828 sources, finding that for 87% of the galaxies, our photometric redshifts were better than $\sigma_z/(1+z) < 0.1$, and for 95% were better than $\sigma_z/(1+z) < 0.2$.

Figure 10 demonstrates the high quality of our photometric redshifts at $z \lesssim 1.5$. Beyond this redshift, spectroscopic surveys have severe limitations due to the intrinsic faintness of the sources (most of them are below the typical $R \sim 25$ spectroscopic limit) and the absence of bright spectroscopic features in the observed optical range for sources at $1.5 \lesssim z \lesssim 2.5$ (the redshift desert). Therefore, photometric redshifts cannot be extensively tested at high z, given that very few spectroscopic redshifts are available. To overcome this problem as much as possible, we included up to 59 galaxies at $z > 1.5$ in our template set, most of them extracted from spectroscopic surveys carried out with spectrographs with enhanced sensitivity in the blue (e.g., Steidel et al. 2004; Reddy et al. 2006a). Using the very few sources with reliable spectroscopic redshifts at $z > 1.5$, our photometric redshifts seem to degrade to some extent. In the HDF-N, 69% of the sources at $z > 1.5$ have photometric redshifts $\sigma_z/(1+z) < 0.2$, and 50% have $\sigma_z/(1+z) < 0.1$. In the CDF-S, 86% of the sources at $z > 1.5$ have photometric redshifts $\sigma_z/(1+z) < 0.2$, and 59% have $\sigma_z/(1+z) < 0.1$.

These statistics are highly biased against red objects, and for blue sources, a very small number of sources is used in the comparison (less than 30 in each field). To further test our results at high z, we analyzed the photometric redshift distribution of samples of galaxies selected with the different color techniques described in § 6. We considered all the IRAC sources identified as LBGs with $R < 25.5$, and DRGs or/and BzK galaxies with $K < 22.9$ (K[Vega] < 21). In § 6, we demonstrate that our IRAC survey detects virtually all these sources (given that the number densities in our sample are very similar to those measured by other surveys focused on the detection of these high-z populations). Here, we test the photometric redshifts derived for these sources, a topic that will be discussed in more detail in a future paper (G. Barro et al. 2008, in preparation).

The average redshift of the LBG-BM sources in our IRAC sample is $\langle z \rangle = 1.4 \pm 0.3$. Both the average and standard deviation values agree, within the typical photometric redshift uncertainties, with the average spectroscopic value of $\langle z \rangle = 1.7 \pm 0.3$ given by Steidel et al. (2004). Reddy et al. (2006a) also find an average $\langle z \rangle = 1.7 \pm 0.3$ for the LBG-BM sources in the HDF-N, where our average photometric redshift is $\langle z \rangle = 1.6 \pm 0.3$. If we calculate the average spectroscopic redshift for the LBG-BM sources in our IRAC sample with available spectroscopy (9% of the total), we obtain $\langle z \rangle = 1.3 \pm 0.3$. Our average is also consistent with the average photometric redshift published by Quadri et al. (2007) for LBG-BM galaxies in MUSYC, $\langle z \rangle = 1.4$, and the first peak of the photometric redshift distribution of LBGs in the GOODS-MUSIC sample (Grazian et al. 2007), also at $z \sim 1.4$.

The average redshift of the LBG-BX sources in our IRAC sample is $\langle z \rangle = 2.0 \pm 0.4$, consistent with the spectroscopic values of $\langle z \rangle = 2.2 \pm 0.3$ found by Steidel et al. (2004) and $\langle z \rangle = 2.2 \pm 0.4$ by Reddy et al. (2006a) in the HDF-N (where we obtain $\langle z \rangle = 2.1 \pm 0.3$). The LBG-BX sources in our sample with available spectroscopy (5% of this subsample) have an average spectroscopic

redshift of $\langle z \rangle = 1.7 \pm 0.4$. Our average is again in perfect agreement with the average photometric redshift published by Quadri et al. (2007) for this population, $\langle z \rangle = 2.1$, and the second peak of the photometric redshift distribution of LBGs in Grazian et al. (2007) placed at $z \sim 2.2$.

The sources in our sample identified as "classical" LBGs lie at an average redshift of $\langle z \rangle = 3.1 \pm 0.5$, which compares well with the spectroscopic values from Steidel et al. (2003, 2004) and Reddy et al. (2006a), all of them being $\langle z \rangle = 3.0 \pm 0.3$. Only 2% of our sources identified as "classical" LBGs have spectroscopy, and the average spectroscopic redshift for them is $\langle z \rangle = 2.5 \pm 1.0$.

The average photometric redshift of the population of DRGs identified in our IRAC survey is $\langle z \rangle = 2.2 \pm 1.0$, and the median is $z = 2.5$, in good agreement (taking into account photometric redshift uncertainties) with the average spectroscopic redshift $\langle z \rangle = 2.5 \pm 0.4$ in the HDF-N (we obtain $\langle z \rangle = 2.4 \pm 0.9$ just in this field) published by Reddy et al. (2005), the median and rms photometric values $z = 2.6 \pm 0.7$ published by Franx et al. (2003), the median photometric redshift $z = 2.2$ from Papovich et al. (2006), and the median photometric redshift $z \sim 2.5$ from Quadri et al. (2007). Spectroscopic redshifts are available for just 4% of the DRGs in our sample, with an average of $\langle z \rangle = 1.5 \pm 0.9$, a lower value than the photometric estimation, probably due to the bias of spectroscopic surveys toward the optically brightest sources (whose probability of being at lower redshifts is relatively larger).

BzK (combining both PE and SF subtypes) sources in our IRAC sample have an average photometric redshift $\langle z \rangle = 2.1 \pm 0.6$, which compares nicely with the average spectroscopic value $\langle z \rangle = 2.1 \pm 0.4$ from Reddy et al. (2005). Other photometric redshift studies obtain similar redshift distribution, e.g., Quadri et al. (2007) and Grazian et al. (2007). The average spectroscopic redshift for BzK sources in our sample (available just for a 1% of the total number of BzK galaxies) is $\langle z \rangle = 1.7 \pm 0.3$.

The previous statistics and the consistency with spectroscopic and photometric values found in the literature demonstrate that our photometric redshifts for the galaxies at $z > 1.5$ are also reliable. Still, a spectroscopic survey focused on high-redshift sources is necessary to increase the reliability (narrow the uncertainties) of our results at $z > 1.5$.

B5.3. *Statistical Evaluation of the Stellar Masses*

In this section, we discuss the quality of our stellar masses, and the possible systematics introduced by our fitting algorithm and the a priori assumptions of the models.

First, we checked how well the minimization algorithm of our SED fitting technique recovered the stellar mass value corresponding to the model best fitting the data. For that purpose, we used 1000 randomly selected galaxies for which we probed all the nodes in the solution grid for the 1-POP case. On average, the difference between the stellar mass estimated with the minimization algorithm and the stellar mass given by the model best fitting the SED is 0.002 dex, the median is 0.000 dex, the standard deviation is 0.07 dex, and there are not any absolute differences larger than 0.20 dex. For the 2-POP case, the number of points in the solution grid is too large to attempt the individual evaluation of all of them. To test this case, we only considered 100 randomly selected galaxies and degraded the resolution of the parameter space grid by one-third for all the free parameters (thus, we only considered 1×10^8 models). On average, the difference between the stellar mass estimated with the minimization algorithm and the stellar mass given by the 2-POP model (with a coarse solution grid) best fitting the SED is 0.04 dex, the median is 0.02 dex, the standard deviation is 0.15 dex, and there are not any absolute differences larger than 0.30 dex. These statistics confirm that the minimization algorithm is able to recover the best stellar mass estimate within the typical uncertainties in stellar populations synthesis analysis (a factor of 2–3).

We also compared the stellar masses obtained with the 1-POP and 2-POP models. For about 70% (55%) of the galaxies, both estimates are equal within a factor of 0.3 dex (0.2 dex). However, for the rest of galaxies (virtually all of them with $M < 10^{10.5}~M_\odot$), the 2-POP estimates are higher (with the most extreme cases showing a difference of up to a factor of 10). On average, including all galaxies, stellar masses derived with 2-POP models are 0.18 dex higher than those derived with 1-POP models. For galaxies with $M > 10^{10.5}~M_\odot$, the average difference is significantly smaller, just 0.02 dex (with a scatter of 0.15 dex). This can be explained by the fact that most of the photometric data points in the modeling fits are found in UV/optical wavelengths, where the emission of relatively young stars is significant. Older stars, possibly much more numerous and dominating the global stellar mass of a galaxy, may be hidden by the intensity of more recent starbursts. This effect should be more noticeable in less massive systems presenting bright recent bursts involving a relatively high fraction (larger than what is normally observed in very massive galaxies with old stellar populations) of the total stellar mass of the galaxy. Only in the 2-POP models are we able to take this effect into account, and that is why in this case we systematically obtain larger stellar masses for some galaxies with relatively low masses. We conclude that the choice of the 1-POP or 2-POP models does not change the stellar masses significantly (more than the typical uncertainties of a factor of 2–3) in a statistical sense, and the effect on the masses for massive galaxies (which dominate the stellar mass density at any redshift) is very small.

Uncertainties in the stellar emission models are known to introduce systematic errors in the estimation of stellar masses from photometry (see, e.g., van der Wel et al. 2006a; van der Wel et al. 2006b). In order to check this effect, the stellar masses obtained with the PEGASE code (Fioc & Rocca-Volmerange 1997) were compared with the values estimated by using the BC03 models from Bruzual & Charlot (2003). On average, the BC03 models give stellar masses larger by 0.03 dex (less than 10%), with a scatter of 0.18 dex. For 95% of the galaxies, the stellar mass difference is lower than a factor of 3. We also fitted the SEDs with the M05 models developed by Maraston 2005 (see also Bruzual 2007), which include a more refined treatment of the emission from thermally pulsating asymptotic giant branch stars, and are claimed to obtain stellar masses that can be lower by as much as 60% (based on the prediction of lower NIR mass-to-light ratios for some ages). On average, the M05 models give stellar masses smaller by 0.14 dex (less than 30%), with a scatter of 0.22 dex (and no clear dependence on redshift). For 96% of the galaxies, the stellar mass difference is lower than a factor of 3.

One important a priori assumption of any stellar population modeling is the treatment of extinction by dust. We compared the stellar masses obtained with the two different extinction recipes we considered (CF00 and CALZ00). For about 80% (65%) of the galaxies, the two estimates are equal within a factor of 0.3 dex (0.2 dex). For the rest of galaxies (again, most of them with $M < 10^{10.5}~M_\odot$), the estimates using the CF00 recipe are higher up to a factor of 5. On average, stellar masses derived with the CF00 recipe are 0.10 dex higher than those derived with CALZ00 law. As discussed in Pérez-González et al. (2003c), in the CF00 recipe the attenuation of the emission arising from the stars is always (except for very young bursts) larger than the attenuation of the gas emission. The CALZ00 recipe shows

an opposite behavior, given that the attenuation of the stellar emission is roughly half of the attenuation of the gas emission. Moreover, the attenuation wavelength dependence (from the UV to the NIR) proposed by CF00 is shallower than the one in CALZ00. This leads to a need for more stars to obtain the same observed luminosity for equal values of the extinction in the CF00 case, which explains the larger stellar masses derived for this case (on average). However, the final effect on the masses is of the order of 0.1 dex, which demonstrates that choice of an extinction recipe does not change the stellar masses more than the typical uncertainties.

Another important assumption of the stellar population models is the IMF, which has a direct effect on the derived stellar masses. Different IMFs produce stellar spectra with very similar colors, but with less or more stars, which causes a systematic uncertainty in the final stellar mass estimations. For example, a Kroupa et al. (1993) IMF (such as the one used in Borch et al. 2006) predicts stellar masses smaller than ours by a factor of ∼1.7, or a Baldry & Glazebrook (2003) IMF (used in, for example, Glazebrook et al. 2004) predicts also smaller masses by a factor of ∼1.8. All our results and those extracted from the literature were normalized to a Salpeter (1955) IMF with $0.1 < M < 100\ M_\odot$. If the IMF is universal (the same at all redshifts), this choice should not affect our results other than in an overall normalization. A discussion of changes in the IMF from galaxy to galaxy is beyond the scope of this paper.

Finally, we performed another test of the goodness of our stellar mass estimates by comparing the results obtained from direct comparison of the SEDs with the entire grid of stellar population models (once the redshift of a galaxy is known) with the results obtained with the photometric redshift technique using the empirically built set of models, from which we obtained stellar mass estimates for all galaxies. We find a very good agreement between these two stellar mass calculations: 90% of galaxies present an average difference between the two mass estimates of less than 0.01 dex, and the scatter around this value is 0.15 dex.

Based on this discussion, the choices of 1-POP or 2-POP models, distinct stellar population libraries, different IMFs, or different extinction recipes produce changes in the derived stellar masses of the same order or smaller than the typical error in any stellar population synthesis analysis (a factor of 2–3), directly linked to the degeneracies of the solutions to the problem. Thus, in the §§ 4 to 7, we only present the results obtained with the stellar masses estimated with the 1-POP models, the Calzetti et al. (2000) extinction law, and a Salpeter (1955) IMF. This choice will also allow us to compare directly with other previous works found in the literature, which usually assume these characteristics in their modeling procedures.

B5.4. *Statistical Evaluation of the SFRs*

In order to understand the systematic and random uncertainties of our estimations of the SFR for each galaxy, we carried out two tests.

First, we used three different dust emission template sets built by Chary & Elbaz (2001), Dale & Helou (2002), and G. H. Rieke et al. (2008, in preparation). The values of the IR SFR [estimated from $L(8$–$1000)$ using the conversion factor found in Kennicutt 1998] derived with the Chary & Elbaz (2001) models were systematically smaller than the SFRs derived with the Dale & Helou (2002) models (on average, 0.1 dex) and G. J. Rieke et al. (2008, in preparation) templates (on average, 0.2 dex). To take into account the systematic uncertainties introduced by the use of a particular set of models, we finally considered an average value of the estimations from the three template sets. The typical uncertainty of this average value (based on the standard deviation of the 3 estimations) is about 50%.

The second test consisted in obtaining IR-based SFRs with different methods. Classically, IR-based SFRs are calculated from the integrated IR luminosity $L(8$–$1000)$. The quantity $L(8$–$1000)$ can be estimated for each galaxy by fitting the IR spectrum with models of the dust emission. For our galaxies, this translates into a significant extrapolation in the templates, since the reddest point in our SEDs corresponds to the observed MIPS 24 μm emission, and we are assuming that a color or a single photometric point in the MIR is closely related to the emission in the FIR, which dominates the integrated IR luminosity. However, one can also avoid this large extrapolation by estimating monochromatic luminosities at specific wavelengths that are not far from the reddest photometric point in our SEDs. In this sense, we estimated monochromatic luminosities at 6.7 μm, 12 μm, and 15 μm, and then calculated the integrated luminosities $L(8$–$1000)$ using the empirical relationships built by Chary & Elbaz (2001). Since they are based on the same templates, these estimations of $L(8$–$1000)$ based on different monochromatic emissions are not independent. However, another independent SFR estimation was obtained by extrapolating in the models to measure the rest-frame MIPS 24 μm monochromatic luminosity. This luminosity was converted to a SFR using the calibration given in Alonso-Herrero et al. (2006). The typical scatter of these different IR-based SFR estimations obtained from monochromatic emissions is 30%.

From these tests, we conclude that our IR-based SFR estimations are good within a factor of 2, which is consistent with other evaluations of IR-based SFRs (e.g., Papovich & Bell 2002; Le Floc'h et al. 2005; Caputi et al. 2006).

B6. EVALUATION OF PARAMETERS DERIVED FOR GALAXIES WITH AGNs

According to § A.6, a small fraction (less than 5%) of our galaxy sample probably harbor an AGN which emits strongly at X-ray and/or IR wavelengths. Given that our goal is to estimate the total stellar mass content of the universe at any redshift up to $z \sim 4$, we must try to keep this type of source in our sample. However, the emission of the dust heated by the nuclear massive black hole can extend to the NIR (if very hot dust, with a temperature of $T \gtrsim 100$ K, is present) and even to optical bands (e.g., in the case of Type 1 QSOs), affecting the estimations of the photometric redshifts, stellar masses, and SFRs.

Given that our photometric redshifts are mainly based on stellar population synthesis models, we can expect that galaxies whose UV-to-NIR SEDs are not stellar are not well represented by our template set, and there is a large probability that the photometric redshift estimation fails. However, only the most extreme and powerful AGNs in our sample would affect the UV-to-NIR global SED of the host galaxy. This is demonstrated by Donley et al. (2007), who build median rest-frame SEDs of X-ray-detected IRAC sources in the HDF-N, finding that only galaxies with X-ray observed luminosities (integrated from 0.5 to 8 keV) $L(X) > 10^{44}$ erg s^{-1} present nonstellar SEDs, and galaxies with $L(X) = 10^{43}$–10^{44} erg s^{-1} start to show significant emission from hot dust at $\lambda_{\rm rest} \gtrsim 2\ \mu$m. Consequently, our stellar mass estimates should only be affected by the presence of an AGN for bright X-ray sources. To further test our stellar masses for AGN, we run a set of stellar population models on 1000 randomly selected galaxies fitting the SED only up to $\lambda_{\rm rest} = 2.3\ \mu$m (the K band) instead of up to $\lambda_{\rm rest} = 4\ \mu$m, to exclude the hot dust emission that can arise at $\lambda_{\rm rest} \sim 2$–$4\ \mu$m (note that only one photometry

data point at most is removed from our SEDs in this case). The average difference between the masses estimated in this way and our original values is just 0.002 dex, and the scatter is 0.10 dex. Cutting the SEDs at even bluer wavelengths, $\lambda_{rest} = 1.5$ μm, has a similar negligible effect: the average difference is 0.004 dex, and the scatter is 0.13 dex. This demonstrates that the (possible) AGN emission in the NIR does not bias our stellar mass estimates for X-ray sources of moderate brightness. For the brightest sources, however, the UV-to-MIR SED is significantly affected by the AGN emission, so we decided to remove from our sample all the X-ray detected sources with $L(X) > 10^{44}$ erg s^{-1}. These sources are just 0.4% of the entire IRAC sample (0.5% of the sample in the HDF-N and the CDF-S, and 0.1% in the LHF), slightly more common at $z > 2$ (1%–2% of all IRAC selected galaxies at high redshift), so they should have a very small additive contribution (not accounted for in our results) on the stellar mass functions and densities.

Concerning the estimation of photometric redshifts, their reliability for X-ray sources is slightly lower than for the global sample: we obtain redshifts with $\sigma_z/(1+z) < 0.1$ for 81% of the X-ray detections, and with $\sigma_z/(1+z) < 0.2$ for 92%. As mentioned above, these sources are very few in comparison with the entire IRAC sample, and they are accounted for in the stellar mass function estimate by using the photometric redshift uncertainties (which are estimated without removing this type of source).

In the case of the SFR estimations, dust-obscured AGNs are expected to radiate the absorbed emission in the MIR/FIR. Although it is common that star formation coexists with AGN activity, it is not possible to decompose the IR emission into the components coming from the two different phenomena, mostly when very few photometric points are available in this wavelength range. Therefore, all X-ray sources were removed in the analysis of the (specific) SFRs carried out in § 7.2. Given that we were only interested in the distribution of specific SFRs of our sample, our results are not significantly affected by the exclusion of this type of source.

REFERENCES

Abraham, R. G., et al. 2007, ApJ, 669, 184
Adelberger, K. L., Steidel, C. C., Shapley, A. E., Hunt, M. P., Erb, D. K., Reddy, N. A., & Pettini, M. 2004, ApJ, 607, 226
Adelman-McCarthy, J. K., et al. 2006, ApJS, 162, 38
Alexander, D. M., et al. 2003, AJ, 126, 539
Alonso-Herrero, A., Rieke, G. H., Rieke, M. J., Colina, L., Pérez-González, P. G., & Ryder, S. D. 2006, ApJ, 650, 835
Alonso-Herrero, A., et al. 2004, ApJS, 154, 155
Arendt, R. G., et al. 1998, ApJ, 508, 74
Armus, L., et al. 2007, ApJ, 656, 148
Baldry, I. K., & Glazebrook, K. 2003, ApJ, 593, 258
Barcons, X., et al. 2002, A&A, 382, 522
Bauer, A. E., Drory, N., Hill, G. J., & Feulner, G. 2005, ApJ, 621, L89
Baugh, C. M., Cole, S., Frenk, C. S., & Lacey, C. G. 1998, ApJ, 498, 504
Baugh, C. M., Lacey, C. G., Frenk, C. S., Granato, G. L., Silva, L., Bressan, A., Benson, A. J., & Cole, S. 2005, MNRAS, 356, 1191
Bell, E. F., & de Jong, R. S. 2001, ApJ, 550, 212
Bell, E. F., McIntosh, D. H., Katz, N., & Weinberg, M. D. 2003, ApJS, 149, 289
Bell, E. F., et al. 2005, ApJ, 625, 23
Benítez, N. 2000, ApJ, 536, 571
Bertin, E., & Arnouts, S. 1996, A&AS, 117, 393
Blain, A. W., Smail, I., Ivison, R. J., Kneib, J.-P., & Frayer, D. T. 2002, Phys. Rep., 369, 111
Bolzonella, M., Miralles, J.-M., & Pelló, R. 2000, A&A, 363, 476
Borch, A., et al. 2006, A&A, 453, 869
Bower, R. G., Benson, A. J., Malbon, R., Helly, J. C., Frenk, C. S., Baugh, C. M., Cole, S., & Lacey, C. G. 2006, MNRAS, 370, 645
Brinchmann, J., & Ellis, R. S. 2000, ApJ, 536, L77
Brocklehurst, M. 1971, MNRAS, 153, 471
Brown, M. J. I., Dey, A., Jannuzi, B. T., Brand, K., Benson, A. J., Brodwin, M., Croton, D. J., & Eisenhardt, P. R. 2007, ApJ, 654, 858
Bruzual A, G. 2007, in ASP Conf. Ser. 374, From Stars to Galaxies, ed. A. Vallenari et al. (San Francisco: ASP), in press (astro-ph/0702091)
Bruzual A, G., & Charlot, S. 2003, MNRAS, 344, 1000
Bundy, K., et al. 2006, ApJ, 651, 120
Burgarella, D., Le Floc'h, E., Takeuchi, T. T., Buat, V., Huang, J. S., Rieke, G. H., & Tyler, K. D. 2007, preprint (astro-ph/0701322)
Burgarella, D., et al. 2006, A&A, 450, 69
Calzetti, D., Armus, L., Bohlin, R. C., Kinney, A. L., Koornneef, J., & Storchi-Bergmann, T. 2000, ApJ, 533, 682
Calzetti, D., et al. 2007, ApJ, 666, 870
Caputi, K. I., et al. 2006, ApJ, 637, 727
Casertano, S., et al. 2000, AJ, 120, 2747
Chabrier, G. 2003, ApJ, 586, L133
Charbonneau, P. 1995, ApJS, 101, 309
Charlot, S., & Fall, S. M. 2000, ApJ, 539, 718
Chary, R., & Elbaz, D. 2001, ApJ, 556, 562
Chen, H., et al. 2003, ApJ, 586, 745
Cole, S., Lacey, C. G., Baugh, C. M., & Frenk, C. S. 2000, MNRAS, 319, 168
Cole, S., et al. 2001, MNRAS, 326, 255
Conselice, C. J., Blackburne, J. A., & Papovich, C. 2005, ApJ, 620, 564
Cowie, L. L., Barger, A. J., Hu, E. M., Capak, P., & Songaila, A. 2004, AJ, 127, 3137

Cowie, L. L., Songaila, A., Hu, E. M., & Cohen, J. G. 1996, AJ, 112, 839
Croton, D. J., et al. 2006, MNRAS, 365, 11
Daddi, E., Cimatti, A., Renzini, A., Fontana, A., Mignoli, M., Pozzetti, L., Tozzi, P., & Zamorani, G. 2004, ApJ, 617, 746
Daddi, E., et al. 2007, ApJ, 670, 173
Dale, D. A., & Helou, G. 2002, ApJ, 576, 159
De Lucia, G., Springel, V., White, S. D. M., Croton, D., & Kauffmann, G. 2006, MNRAS, 366, 499
Dey, A., Graham, J. R., Ivison, R. J., Smail, I., Wright, G. S., & Liu, M. C. 1999, ApJ, 519, 610
Dickinson, M., Giavalisco, M., & The Goods Team. 2003a, in The Mass of Galaxies at Low and High Redshift, ed. R. Bender & A. Renzini (Berlin: Springer), 324
Dickinson, M., Papovich, C., Ferguson, H. C., & Budavári, T. 2003b, ApJ, 587, 25
Dickinson, M., et al. 2000, ApJ, 531, 624
Donley, J. L., Rieke, G. H., Pérez-González, P. G., Rigby, J. R., & Alonso-Herrero, A. 2007, ApJ, 660, 167
Donley, J. L., Rieke, G. H., Rigby, J. R., & Pérez-González, P. G. 2005, ApJ, 634, 169
Drory, N., Bender, R., Feulner, G., Hopp, U., Maraston, C., Snigula, J., & Hill, G. J. 2004, ApJ, 608, 742
Drory, N., Salvato, M., Gabasch, A., Bender, R., Hopp, U., Feulner, G., & Pannella, M. 2005, ApJ, 619, L131
Efstathiou, G., Ellis, R. S., & Peterson, B. A. 1988, MNRAS, 232, 431
Eisenhardt, P. R., et al. 2004, ApJS, 154, 48
Elmegreen, B. G. 2004, MNRAS, 354, 367
Elston, R., Rieke, G. H., & Rieke, M. J. 1988, ApJ, 331, L77
Fazio, G. G., et al. 2004a, ApJS, 154, 39
———. 2004b, ApJS, 154, 10
Ferland, G. J. 1980, PASP, 92, 596
Fioc, M., & Rocca-Volmerange, B. 1997, A&A, 326, 950
Fontana, A., et al. 2003, ApJ, 594, L9
———. 2004, A&A, 424, 23
———. 2006, A&A, 459, 745
Förster Schreiber, N. M., et al. 2004, ApJ, 616, 40
Franceschini, A., Aussel, H., Cesarsky, C. J., Elbaz, D., & Fadda, D. 2001, A&A, 378, 1
Franx, M., et al. 2003, ApJ, 587, L79
Fukugita, M., Hogan, C. J., & Peebles, P. J. E. 1998, ApJ, 503, 518
Gawiser, E., et al. 2006, ApJS, 162, 1
Giacconi, R., et al. 2002, ApJS, 139, 369
Gil de Paz, A., & Madore, B. F. 2002, AJ, 123, 1864
Glazebrook, K., et al. 2003, ApJ, 587, 55
———. 2004, Nature, 430, 181
Gordon, K. D., et al. 2005, PASP, 117, 503
Granato, G. L., De Zotti, G., Silva, L., Bressan, A., & Danese, L. 2004, ApJ, 600, 580
Grazian, A., et al. 2006, A&A, 449, 951
———. 2007, A&A, 465, 393
Hasinger, G., et al. 2001, A&A, 365, L45
Heavens, A., Panter, B., Jimenez, R., & Dunlop, J. 2004, Nature, 428, 625
Hopkins, A. M. 2004, ApJ, 615, 209
Hopkins, A. M., & Beacom, J. F. 2006, ApJ, 651, 142

Huang, J.-S., et al. 2004, ApJS, 154, 44
———. 2005, ApJ, 634, 137
Hughes, D. H., et al. 1998, Nature, 394, 241
Ilbert, O., et al. 2004, MNRAS, 351, 541
Im, M., Yamada, T., Tanaka, I., & Kajisawa, M. 2002, ApJ, 578, L19
Jimenez, R., Bernardi, M., Haiman, Z., Panter, B., & Heavens, A. F. 2007, ApJ, 669, 947
Juneau, S., et al. 2005, ApJ, 619, L135
Kauffmann, G., White, S. D. M., & Guiderdoni, B. 1993, MNRAS, 264, 201
Kauffmann, G., et al. 2003, MNRAS, 341, 33
Kennicutt, R. C. 1998, ARA&A, 36, 189
Klessen, R. S., Spaans, M., & Jappsen, A.-K. 2007, MNRAS, 374, L29
Kochanek et al. 2001, ApJ, 560, 566
Kron, R. G. 1980, ApJS, 43, 305
Kroupa, P. 2007, in Pathways through an Eclectic Universe, ed. J. H. Knapen, T. J. Mahoney, & A. Vazdekis, in press (arXiv:0708.1164)
Kroupa, P., Tout, C. A., & Gilmore, G. 1993, MNRAS, 262, 545
Labbé, I., et al. 2003, AJ, 125, 1107
———. 2005, ApJ, 624, L81
Lacey, C. G., Baugh, C. M., Frenk, C. S., Silva, L., Granato, G. L., & Bressan, A. 2007, MNRAS, submitted (arXiv:0704.1562)
Larson, R. B. 1998, MNRAS, 301, 569
Lawrence, A., et al. 2007, MNRAS, 379, 1599
Le Delliou, M., Lacey, C. G., Baugh, C. M., & Morris, S. L. 2006, MNRAS, 365, 712
Le Fèvre, O., et al. 2004, A&A, 428, 1043
Le Floc'h, E., et al. 2004, ApJS, 154, 170
———. 2005, ApJ, 632, 169
Lehmann, I., et al. 2000, A&A, 354, 35
Lilly, S. J., Le Fevre, O., Hammer, F., & Crampton, D. 1996, ApJ, 460, L1
Loveday, J. 2000, MNRAS, 312, 557
Madau, P., Ferguson, H. C., Dickinson, M. E., Giavalisco, M., Steidel, C. C., & Fruchter, A. 1996, MNRAS, 283, 1388
Mainieri, V., Bergeron, J., Hasinger, G., Lehmann, I., Rosati, P., Schmidt, M., Szokoly, G., & Della Ceca, R. 2002a, A&A, 393, 425
Mainieri, V., Bergeron, J., Rosati, P., Hasinger, G., & Lehmann, I. 2002b, preprint (astro-ph/0202211)
Maness, H., et al 2007, ApJ, 669, 1024
Maraston, C. 2005, MNRAS, 362, 799
Marchesini, D., et al. 2007, ApJ, 656, 42
Nagamine, K., Cen, R., Hernquist, L., Ostriker, J. P., & Springel, V. 2004, ApJ, 610, 45
———. 2005a, ApJ, 627, 608
———. 2005b, ApJ, 618, 23
Nagamine, K., Ostriker, J. P., Fukugita, M., & Cen, R. 2006, ApJ, 653, 881
Nagashima, M., Lacey, C. G., Okamoto, T., Baugh, C. M., Frenk, C. S., & Cole, S. 2005, MNRAS, 363, L31
Osterbrock, D. E. 1989, Astrophysics of Gaseous Nebulae and Active Galactic Nuclei (Mill Valley: University Science Books)
Pérez-González, P. G., Gallego, J., Zamorano, J., Alonso-Herrero, A., Gil de Paz, A., & Aragón-Salamanca, A. 2003a, ApJ, 587, L27
Pérez-González, P. G., Gil de Paz, A., Zamorano, J., Gallego, J., Alonso-Herrero, A., & Aragón-Salamanca, A. 2003b, MNRAS, 338, 508
———. 2003c, MNRAS, 338, 525
Pérez-González, P. G., et al. 2005, ApJ, 630, 82
Padoan, P., Nordlund, A., & Jones, B. J. T. 1997, MNRAS, 288, 145
Pannella, M., Hopp, U., Saglia, R. P., Bender, R., Drory, N., Salvato, M., Gabasch, A., & Feulner, G. 2006, ApJ, 639, L1
Papovich, C., & Bell, E. F. 2002, ApJ, 579, L1

Papovich, C., et al. 2006, ApJ, 640, 92
———. 2007, ApJ, 668, 45
Quadri, R., et al. 2007, AJ, 134, 1103
Reach, W. T., et al. 2005, PASP, 117, 978
Reddy, N. A., Erb, D. K., Steidel, C. C., Shapley, A. E., Adelberger, K. L., & Pettini, M. 2005, ApJ, 633, 748
Reddy, N. A., Steidel, C. C., Erb, D. K., Shapley, A. E., & Pettini, M. 2006a, ApJ, 653, 1004
Reddy, N. A., Steidel, C. C., Fadda, D., Yan, L., Pettini, M., Shapley, A. E., Erb, D. K., & Adelberger, K. L. 2006b, ApJ, 644, 792
Reddy, N. A., Steidel, C. C., Pettini, M., Adelberger, K. L., Shapley, A. E., Erb, D. K., & Dickinson, M. 2007, ApJ, submitted (arXiv:0706.4091)
Rigby, J. R., et al. 2004, ApJS, 154, 160
Rowan-Robinson, M., et al. 2005, AJ, 129, 1183
Rudnick, G., et al. 2006, ApJ, 650, 624
Salpeter, E. E. 1955, ApJ, 121, 161
Salucci, P., & Persic, M. 1999, MNRAS, 309, 923
Schechter, P. 1976, ApJ, 203, 297
Schiminovich, D., et al. 2005, ApJ, 619, L47
Shapley, A. E., Steidel, C. C., Erb, D. K., Reddy, N. A., Adelberger, K. L., Pettini, M., Barmby, P., & Huang, J. 2005, ApJ, 626, 698
Silk, J. 2005, MNRAS, 364, 1337
Smail, I., Ivison, R. J., & Blain, A. W. 1997, ApJ, 490, L5
Somerville, R. S., Primack, J. R., & Faber, S. M. 2001, MNRAS, 320, 504
Steidel, C. C., Adelberger, K. L., Shapley, A. E., Pettini, M., Dickinson, M., & Giavalisco, M. 2003, ApJ, 592, 728
Steidel, C. C., Shapley, A. E., Pettini, M., Adelberger, K. L., Erb, D. K., Reddy, N. A., & Hunt, M. P. 2004, ApJ, 604, 534
Szokoly, G. P., et al. 2004, ApJS, 155, 271
Tozzi, P., et al. 2006, A&A, 451, 457
Tresse, L., et al. 2007, A&A, 472, 403
Treu, T., et al. 2005, ApJ, 633, 174
van der Wel, A., Franx, M., van Dokkum, P. G., Huang, J., Rix, H.-W., & Illingworth, G. D. 2006a, ApJ, 636, L21
van der Wel, A., Franx, M., van Dokkum, P. G., Rix, H.-W., Illingworth, G. D., & Rosati, P. 2005, ApJ, 631, 145
van der Wel, A., Franx, M., Wuyts, S., van Dokkum, P. G., Huang, J., Rix, H.-W., & Illingworth, G. D. 2006b, ApJ, 652, 97
van Dokkum, P. G. 2005, AJ, 130, 2647
van Dokkum, P. G., et al. 2003, ApJ, 587, L83
———. 2006, ApJ, 638, L59
van Dokkum, P. G., & van der Marel, R. P. 2007, ApJ, 655, 30
Vanzella, E., et al. 2005, A&A, 434, 53
———. 2006, A&A, 454, 423
Wainscoat, R. J., Cohen, M., Volk, K., Walker, H. J., & Schwartz, D. E. 1992, ApJS, 83, 111
Webb, T. M. A., et al. 2006, ApJ, 636, L17
Werner, M. W., et al. 2004, ApJS, 154, 1
Willmer, C. N. A. 1997, AJ, 114, 898
Wirth, G. D., et al. 2004, AJ, 127, 3121
Yan, L., McCarthy, P. J., Weymann, R. J., Malkan, M. A., Teplitz, H. I., Storrie-Lombardi, L. J., Smith, M., & Dressler, A. 2000, AJ, 120, 575
Yuan, W., McMahon, R. G., Watson, M., Tedds, J., Motch, C., Schwope, A., & the XMM Survey Science Center team. 2003, Astron. Nachr., 324, 178
Zappacosta, L., Maiolino, R., Finoguenov, A., Mannucci, F., Gilli, R., & Ferrara, A. 2005, A&A, 434, 801
Zheng, X. Z., Bell, E. F., Papovich, C., Wolf, C., Meisenheimer, K., Rix, H.-W., Rieke, G. H., & Somerville, R. 2007, ApJ, 661, L41